Electrohydrodynamic Stability

Chuan-Hua Chen*
Department of Mechanical Engineering and Materials Science,
Duke University, Durham, NC, USA

Abstract Stability of electrohydrodynamic flows is essential to a variety of applications ranging from electrokinetic assays to electrospray ionization. In this series of lecture notes, a few basic concepts of electrohydrodynamic stability are illustrated using two model problems, electrokinetic mixing flow and electrohydrodynamic cone-jet, respectively wall-bounded and free surface flow. After a review of the governing equations, spatiotemporal analysis of the two example problems is presented using linearized bulk- or surface-coupled models. The operating regimes for these flows are discussed within the framework of electrohydrodynamic stability.

1 Introduction

Electrohydrodynamic transport phenomena are fundamental to a variety of engineering applications such as electrokinetic assays, electrospray ionization, electro-coalescence and mixing, electrostatic printing and spinning. Although unstable flow is desired in certain applications (e.g. in mixing), a stable flow is typically the preferred state (e.g. in assays and ionization). In either case, the demarcation between the stable and unstable states is of practical importance. The theme of these lecture notes is to develop a systematic methodology in identifying such stability boundaries of electrohydrodynamic flows. The topics have been selected mainly for their pedagogical value in illustrating the basic concepts in continuum electromechanics and hydrodynamic stability, often motivated by practical applications and backed by experimental observations. Although the governing equations and analysis methodology should be of general applicability, no attempt

*I am indebted to the organizer, Dr. A. Ramos, who graciously helped on delivering the videotaped lectures as a result of visa complications that prevented me from traveling to CISM. My Ph.D. adviser J. G. Santiago helped on the initial outline of the lecture notes. Drs. M. P. Brenner and A. M. Ganan-Calvo provided helpful correspondence about their research. This work was funded in part by an NSF CAREER Award.

A. Ramos (ed.), *Electrokinetics and Electrohydrodynamics in Microsystems*

has been made to comprehensively review the rapidly expanding field of electrohydrodynamic stability. Extensive coverage of electrohydrodynamics and the associated flow stability can be found in Melcher and Taylor (1969); Melcher (1981); Saville (1997); Fernandez de la Mora (2007); Chang and Yeo (2010). In addition, an educational film developed by Melcher (1974) offers many intuitive insights on electrohydrodynamics.

2 Basics of Electrohydrodynamics

Electrohydrodynamics deals with the interaction of electric and flow fields where the Ohmic model is frequently an excellent approximation (Melcher and Taylor, 1969; Saville, 1997). In this section, we first present an intuitive derivation of the Ohmic model and clearly identify the assumptions behind. We then offer some physical insights on the Maxwell stress tensor which plays the crucial role of coupling the electrostatics and hydrodynamics. Finally, we discuss the governing equations for both surface- and bulk-coupled models. The surface-coupled model takes essentially the same form as in Melcher and Taylor (1969) and Saville (1997), while the bulk-coupled model takes roots in Levich (1962) and Melcher (1981).

2.1 Ohmic model

Electrohydrodynamic systems can usually be approximated as electroquasistatic (Saville, 1997). In the absence of external magnetic fields, magnetic effects can be ignored completely. The electrostatic field is solenoidal,

$$\nabla \times \mathbf{E} = 0. \tag{1}$$

The electric field ($\mathbf{E}$) obeys the Gauss's law, which for electrically linear medium reduces to,

$$\nabla \cdot \varepsilon \mathbf{E} = \rho_f, \tag{2}$$

where ε is the permittivity, and ρ_f is the free charge density. The free charge density is related to the current ($\mathbf{i}$) by the charge conservation equation,

$$\frac{\partial \rho_f}{\partial t} + \nabla \cdot \mathbf{i} = 0. \tag{3}$$

In the Ohmic model, or the so-called leaky dielectric model (Saville, 1997), an Ohmic constitutive law of the conduction current is assumed (Melcher and Taylor, 1969),

$$\mathbf{i} = \mathbf{i}_C + \mathbf{i}_O = \rho_f \mathbf{v} + \sigma \mathbf{E}, \tag{4}$$

where $\mathbf{i}_C = \rho_f \mathbf{v}$ is the convection current, $\mathbf{i}_O = \sigma \mathbf{E}$ is the Ohmic current, $\mathbf{v}$ is the fluid velocity, and σ is the electrical conductivity. The Ohmic model can be derived from the electro-diffusive transport of individual charged ions (Melcher, 1981; Saville, 1997; Levich, 1962). We assume for algebraic simplicity a monovalent binary electrolyte which is fully dissociated with constant properties (Chen et al., 2005). For derivations involving multivalent electrolyte and chemical reaction, see Levich (1962) and Saville (1997), respectively. In the Ohmic model, bulk quantities of conductivity and charge density are tracked instead of individual ions. The charge density (ρ_f) and electric conductivity (σ) are related to the ionic concentrations through

$$\rho_f = F(c_+ - c_-), \tag{5}$$

$$\sigma = F^2(c_+ m_+ + c_- m_-), \tag{6}$$

where F is the Faraday constant, $c_\pm$ is the cationic/anionic molar concentration, and $m_\pm$ is the ionic mobility (in $\mathrm{mol\,N^{-1}\,m\,s^{-1}}$).

The key simplifying assumption in the derivation is electro-neutrality, which can be assumed in the limit of (Chen et al., 2005)

$$\Theta_1 = \frac{F m_+ \rho_f}{\sigma} = \frac{c_+ - c_-}{c_+ + \frac{m_-}{m_+} c_-} \ll 1, \tag{7}$$

where Θ_1 represents the ratio of cationic and anionic concentration difference (which contributes to the charge density) to the total concentration of ions (which contributes to the electrical conductivity). Applying the Gauss's law,

$$\Theta_1 = \frac{F m_+ \rho_f}{\sigma} \sim \frac{F m_+ \nabla \cdot \varepsilon \mathbf{E}}{\sigma} \sim \frac{\varepsilon/\sigma}{L_r/m_+ FE} \sim \frac{\tau_e}{\tau_r}, \tag{8}$$

where $\tau_e = \varepsilon/\sigma$ is the charge relaxation time, $m_+ FE$ is by definition the electro-migration velocity of the cation, L_r is a reference length scale over which the electric field varies (typically the smallest length scale of the electrohydrodynamic system), and τ_r is the time scale to travel L_r by electromigration. Therefore, electro-neutrality is an excellent approximation for most electrolyte solutions (typically with $\sigma > 10^{-4}$ S/m) with fast charge relaxation (typically with $\tau_e < 10\ \mu$s), because the charge relaxation time is much shorter than the electrohydrodynamic time scale of interest (typically with $\tau_r > 1$ ms). When the electrolyte solution is approximately neutral,

$$c_+ \simeq c_- = c; \quad |\, c_+ - c_- \,| \ll c, \tag{9}$$

where c is the reduced ionic concentration (Levich, 1962). Under electroneutrality, the conductivity is proportional to this reduced concentration by

$$\sigma = F^2(m_+ + m_-)c. \tag{10}$$

To derive the governing equation for conductivity, we start from the Nernst-Planck equations for ionic species (Levich, 1962),

$$\frac{\partial c_+}{\partial t} + \nabla \cdot c_+\mathbf{v} = D_+\nabla^2 c_+ - m_+F\nabla \cdot c_+\mathbf{E}, \tag{11}$$

$$\frac{\partial c_-}{\partial t} + \nabla \cdot c_-\mathbf{v} = D_-\nabla^2 c_- + m_-F\nabla \cdot c_-\mathbf{E}, \tag{12}$$

where $D_\pm$ is the ionic diffusivity. The diffusivity and mobility is related by Einstein's relation $D_\pm = RTm_\pm$ where R is the universal gas constant and T is the absolute temperature. Subtracting Eqs. 11 and 12 and noting the electro-neutrality condition,

$$(D_+ + D_-)F\nabla \cdot c\mathbf{E} \simeq RT(D_+ - D_-)\nabla^2 c, \tag{13}$$

where the equality holds to the leading order of ionic concentrations. Substituting Eq. 13 to Eq. 11 and noting Eq. 10, the electro-diffusion equation becomes

$$\frac{\partial \sigma}{\partial t} + \nabla \cdot \sigma\mathbf{v} = D_{eff}\nabla^2\sigma, \tag{14}$$

where D_{eff} is an effective diffusivity,

$$D_{eff} = \frac{2D_+D_-}{D_+ + D_-}. \tag{15}$$

To derive the equation for charge density, we subtract Eqs. 11 and 12 again in an exact manner,

$$\frac{\partial(c_+ - c_-)}{\partial t} + \nabla\cdot(c_+ - c_-)\mathbf{v} = \nabla^2(D_+c_+ - D_-c_-) - F\nabla\cdot(m_+c_+ + m_-c_-)\mathbf{E}, \tag{16}$$

or in terms of bulk quantities,

$$\frac{\partial \rho_f}{\partial t} + \nabla \cdot (\rho_f\mathbf{v} + \mathbf{i}_D + \sigma\mathbf{E}) = 0, \tag{17}$$

where the diffusive current $\mathbf{i}_D = -F\nabla(D_+c_+ - D_-c_-) \simeq -(D_+ - D_-)F\nabla c$ (Levich, 1962). Eq. 17 reduces to the the charge conservation equation in the Ohmic regime,

$$\frac{\partial \rho_f}{\partial t} + \nabla \cdot \rho_f\mathbf{v} = -\nabla \cdot \sigma\mathbf{E}, \tag{18}$$

when the diffusive current can be neglected, i.e.

$$\Theta_2 = \left| \frac{\mathbf{i}_D}{\mathbf{i}_O} \right| \ll 1. \tag{19}$$

In electrohydrodynamic systems, the diffusive current is usually much smaller than the Ohmic conduction current. The ratio of the two currents scales as,

$$\Theta_2 = \left| \frac{\mathbf{i}_D}{\mathbf{i}_O} \right| \sim \frac{(D_+ - D_-)F\nabla c}{(m_+ + m_-)F^2 cE} \sim \frac{D_+ - D_-}{D_+ + D_-} \frac{RT}{F} \frac{\nabla c}{Ec} \sim \frac{RT/F}{EL_r} \sim \frac{\Phi_T}{\Phi_r}, \tag{20}$$

where $\Phi_T = RT/F$ (25 mV at room temperature) is the thermal voltage driving the diffusive current, and Φ_r is the reference voltage drop along a concentration gradient. Since the applied electric field is typically high in an electrohydrodynamic system, the diffusive current can be safely neglected (i.e. Eq. 19 is valid) for most practical cases. For example, with a field of 10^5 V/m, $\Theta_2 \ll 1$ for a diffusive interface as thin as 1 μm.

The Ohmic model consists of the conservation equations for conductivity (Eq. 14) and charge density (Eq. 18). Physically, the material derivative of conductivity and charge density is balanced by the divergence of an effective diffusive flux and Ohmic current flux, respectively. The underlying assumptions in the Ohmic model are instantaneous charge relaxation (Eq. 7) and negligible diffusive current (Eq. 19).[1] Both assumptions hold for most practical electrohydrodynamic systems driven by direct-current (DC) fields, where the time scale of interest is typically above 1 ms and the length scale of interest is typically above 1 μm. With rapid charge relaxation, the electrolyte solution is approximately electro-neutral in the bulk and the cations and anions are almost always paired together, as the difference in cationic and ionic concentrations is very small compared to the background concentration of electrolytes. Consequently, conductivity becomes a conserved material property with an effective diffusivity averaging the cationic and anionic properties. Note that the Ohmic model does not work inside electric double layer, where the net charged layer has a typical thickness of well below 1 μm.

2.2 Maxwell stress

The electrostatics and hydrodynamics are coupled together through the Maxwell stress tensor. In vacuum, the Coulombic force density exerted on

[1] Although we have assumed constant properties ($D_\pm$ and $m_\pm$) in the derivation, the Ohmic model consisting of Eqs. 14 and 18 are generally believed to hold for cases with non-constant properties, e.g. due to temperature gradients.

free charges can be rearranged noting the solenoidal nature of the electrostatic field (Panofsky and Phillips, 1962),

$$\begin{aligned}\mathbf{f}_0^e &= \rho_f \mathbf{E} = (\nabla \cdot \varepsilon_0 \mathbf{E})\mathbf{E} \\ &= \nabla \cdot \left(\varepsilon_0 \mathbf{E}\mathbf{E} - \frac{1}{2}\varepsilon_0 E^2 \mathbf{I} \right) = \nabla \cdot \mathbf{T}_0^e, \end{aligned} \tag{21}$$

where ε_0 is the permittivity of vacuum, $\mathbf{I}$ is the identity matrix, and $\mathbf{T}_0^e$ is the Maxwell stress (or electric stress) tensor in vacuum.

The derivation of Maxwell stress tensor for a dielectric medium is rather complicated (Melcher, 1981; Panofsky and Phillips, 1962). Here, we summarize salient points of the Maxwell stress tensor and refer the readers to Melcher (1981) for details. The electrical force density can be derived using either the Kelvin approach or the Korteweg-Helmholtz approach. The Kelvin force density is useful for appreciating the underlying microscopic electromechanics, while the Korteweg-Helmholtz force density is more useful for predicting the consequences of electromechanical coupling (Melcher, 1974). The Kelvin force density is the sum of the Coulombic force exerted on free charges and the polarization force exerted on the dipoles (Melcher, 1981),

$$\begin{aligned}\mathbf{f}_K^e &= \rho_f \mathbf{E} + \mathbf{P} \cdot \nabla \mathbf{E} = (\nabla \cdot \varepsilon \mathbf{E})\, \mathbf{E} + (\varepsilon - \varepsilon_0)\, \mathbf{E} \cdot \nabla \mathbf{E} \\ &= \nabla \cdot \left(\varepsilon \mathbf{E}\mathbf{E} - \frac{1}{2}\varepsilon_0 E^2 \mathbf{I} \right) = \nabla \cdot \mathbf{T}_K^e, \end{aligned} \tag{22}$$

where $\mathbf{P}$ is the polarization density, and $\mathbf{T}_K^e$ is the Maxwell stress tensor corresponding to the Kelvin force density. The key concept due to Kelvin is that the polarization force is exerted on the dipoles ($\mathbf{P}$), not on individual polarization charges ($-\nabla \cdot \mathbf{P}$) (Melcher, 1981). The Korteweg-Helmholtz force density stems from thermodynamic principles. For an electrically linear medium with polarization dependent on mass density (ρ) and temperature (T) alone, the force density can be shown to be,

$$\begin{aligned}\mathbf{f}_{KH}^e &= \rho_f \mathbf{E} - \frac{1}{2}E^2 \nabla \varepsilon + \nabla \left[\frac{1}{2}\rho \left(\frac{\partial \varepsilon}{\partial \rho} \right)_T E^2 \right] \\ &= \nabla \cdot \left[\varepsilon \mathbf{E}\mathbf{E} - \frac{1}{2}\varepsilon E^2 \mathbf{I} + \frac{1}{2}\rho \left(\frac{\partial \varepsilon}{\partial \rho} \right)_T E^2 \mathbf{I} \right] = \nabla \cdot \mathbf{T}_{KH}^e, \end{aligned} \tag{23}$$

where the last term is the electrostriction force density associated with volumetric change in the material; See Melcher (1981, Sec. 3.7) for a detailed derivation. The Kelvin and Korteweg-Helmholtz force densities are different

by the gradient of a scalar,

$$\mathbf{f}_K^e - \mathbf{f}_{KH}^e = \nabla \left[\frac{1}{2}(\varepsilon - \varepsilon_0)E^2 - \frac{1}{2}\rho \left(\frac{\partial \varepsilon}{\partial \rho} \right)_T E^2 \right], \tag{24}$$

which can be absorbed into a lumped pressure. The difference represents the interaction between dipoles, which is omitted in the Kelvin derivation. For incompressible flow, where pressure becomes a "left-over" variable, any two force densities differing by the gradient of a scalar pressure will give rise to the same incompressible deformation (Melcher, 1981). Both force densities, if used consistently, will yield the same answer as far as incompressible mechanical deformation is concerned. Because the actual electric force distributions of the two approaches are ususally very different, we stress that the same force density should be used consistently; See an example in Melcher (1981, Sec. 8.3).

Hereon, we shall restrict our discussions to the practically important case of *electrically linear, incompressible* dielectric medium, and *consistently* adopt the Korteweg-Helmholtz force density,

$$\begin{aligned} \mathbf{f}^e &= \rho_f \mathbf{E} - \frac{1}{2}E^2 \nabla \varepsilon \\ &= \nabla \cdot \left(\varepsilon \mathbf{E}\mathbf{E} - \frac{1}{2}\varepsilon E^2 \mathbf{I} \right) = \nabla \cdot \mathbf{T}^e. \end{aligned} \tag{25}$$

When the permittivity is that of vacuum, the Maxwell stress tensor $\mathbf{T}^e$ in Eq. 25 reduces to $\mathbf{T}_0^e$ in Eq. 21. This similarity enables us to take advantage of the "bisect rule" graphically shown in Figure 1 (Panofsky and Phillips, 1962, Sec. 6-5). The bisect rule is useful in graphically identifying the direction of electric stress when the field direction is known. A few example applications of the bisect rule are shown in Figure 2.

From the Korteweg-Helmholtz force density in Eq. 25 and the corresponding bisect rule in Figure 2, it is apparent why a leaky dielectric is necessary to support any tangential electric stress at electrostatic interfaces (Melcher and Taylor, 1969). For a perfect conductor such as the charged drop in (a), the Coulombic force is always along the electric field which is perpendicular to the interface. For a perfect dielectric such as a dielectric jet in (b), the polarization force is always along the permittivity gradient which is again perpendicular to the interface. For a leaky dielectric with finite, non-zero conductivity and permittivity, a tangential shear stress can develop such as in the electrified cone in (c), where the electric field at 45° to the surface normal gives rise to a shear force along the conical surface.

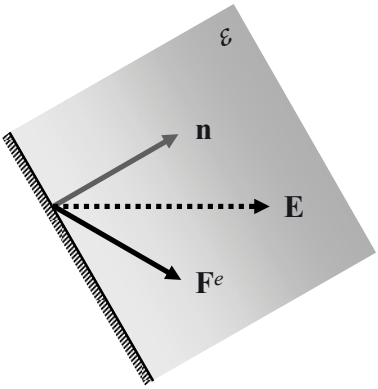

Figure 1. The bisect rule: the electric field (**E**) bisects the angel between the normal to the surface (**n**) and the direction of the resultant force ($\mathbf{F}^e$) acting on the surface (dS). In a dielectric medium with a local permittivity of ε, the magnitude of the electric force is $F^e = T^e dS = \frac{1}{2}\varepsilon E^2 dS$. After Panofsky and Phillips (1962).

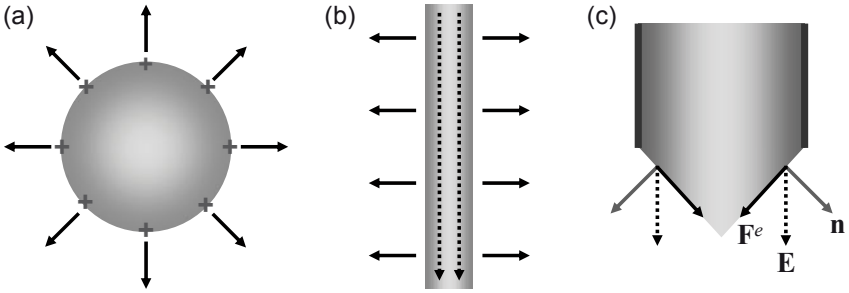

Figure 2. Example applications of the bisect rule: (a) on a charged conducting drop, the surface normal is along the direction of the electric field, hence the Coulombic repulsion is also along the direction of the electric field; (b) on a dielectric liquid jet, the surface normal is perpendicular to the electric field, hence the polarization force is perpendicular to the electric field and pointing outward; (c) on a leaky dielectric cone, the surface normal is at 45° to the electric field, hence the (total) electric force is along the tangential direction of the cone which is also at 45° to the electric field.

2.3 Governing equations

To summarize, the electrohydrodynamic leaky dielectric model consists of the following equations:

$$\nabla \times \mathbf{E} = 0, \tag{26a}$$

$$\nabla \cdot \varepsilon \mathbf{E} = \rho_f, \tag{26b}$$

$$\frac{\partial \rho_f}{\partial t} + \nabla \cdot \rho_f \mathbf{v} = -\nabla \cdot \sigma \mathbf{E}. \tag{26c}$$

$$\nabla \cdot \mathbf{v} = 0, \tag{26d}$$

$$\rho \frac{\partial \mathbf{v}}{\partial t} + \rho \mathbf{v} \cdot \nabla \mathbf{v} = -\nabla p + \mu \nabla^2 \mathbf{v} + \rho_f \mathbf{E} - \frac{1}{2} E^2 \nabla \varepsilon, \tag{26e}$$

where p is the pressure and μ is the dynamic viscosity. The electric body forces in the momentum equation (Eq. 26e) include both a Coulombic and a polarization component. These equations are valid for incompressible, electrically linear leaky dielectrics with rapid charge relaxation and negligible diffusive current, for example, aqueous electrolyte solutions. The set of governing equations (26) is closed if the distribution of material properties (ε, σ, μ) is either given or modeled with additional equations.

We have employed the electro-neutrality assumption in the derivation of the Ohmic model, but kept the charge density in the governing equations. Although the material derivative of ρ_f may often be neglected in the charge conservation equation (Eq. 26c), it will not be appropriate to neglect the Coulombic body force term $\rho_f \mathbf{E}$ in the momentum equation (Eq. 26e) because this force *drives* the electrohydrodynamic flow. Combining the charge conservation equation (Eq. 26c) and the Gauss's law (Eq. 26b) (Melcher, 1974),

$$\frac{D\rho_f}{Dt} = \frac{\rho_f}{\tau_e} - \sigma \mathbf{E} \cdot \left(\frac{\nabla \sigma}{\sigma} - \frac{\nabla \varepsilon}{\varepsilon} \right). \tag{27}$$

In regions of uniform conductivity and permittivity, the net free charge decays with the charge relaxation time for an observer following a particle of fixed identity (Melcher and Taylor, 1969):

$$\rho_f = \rho_{f,0} e^{-t/\tau_e}. \tag{28}$$

Therefore, unless an element of material having uniform properties can be traced along a particle line to a source of net charge, it supports no net charge (Melcher and Taylor, 1969). In inhomogeneous material, however, free charge density can be generated by an electric field component along the gradients of conductivity and/or permittivity.

Systems having nonuniform properties can be modeled either as a bulk region with continuously varying properties or as adjoining regions with piecewise uniform properties (Melcher, 1981; Hoburg and Melcher, 1976). Since interesting electrohydrodynamics often happen at material interfaces, we shall discuss two approaches to close the problem depending on the interfacial sharpness (Hoburg and Melcher, 1976).

In the bulk-coupled model for a diffusive interface, additional equations of the materials properties must be added. For example, in aqueous electrolytes the permittivity is essentially constant but the conductivity variation can be significant; in this case, the "conservation" equation of conductivity from the Ohmic model can be used,

$$\frac{\partial \sigma}{\partial t} + \nabla \cdot \sigma \mathbf{v} = D_{eff} \nabla^2 \sigma. \tag{29}$$

In the surface-coupled model for a sharp interface, the material properties are usually piecewise constant on either side of the interface; However, jump conditions are needed to relate the interfacial and bulk properties. Except for the empirical no-slip condition (Eq. 30e), the following jump conditions can be obtained by integrating the differential equations across the interface (Melcher and Taylor, 1969; Melcher, 1981; Saville, 1997; Leal, 2007),

$$\mathbf{n} \times \|\mathbf{E}\| = 0, \tag{30a}$$

$$\mathbf{n} \cdot \|\varepsilon \mathbf{E}\| = q_s, \tag{30b}$$

$$\frac{\partial q_s}{\partial t} + \nabla_s \cdot (q_s \mathbf{v}) = -\mathbf{n} \cdot \|\sigma \mathbf{E}\|, \tag{30c}$$

$$\mathbf{n} \cdot \|\mathbf{v}\| = 0, \tag{30d}$$

$$\mathbf{n} \times \|\mathbf{v}\| = 0, \tag{30e}$$

$$\mathbf{n} \|p\| = \mathbf{n} \cdot \|\mathbf{T}^m + \mathbf{T}^e\| + \nabla_s \gamma - \gamma \mathbf{n} (\nabla_s \cdot \mathbf{n}), \tag{30f}$$

where $\|\,.\,\|$ denotes the jump in a variable across the interface, $\mathbf{n}$ denotes the outward normal vector, subscript s denotes surface quantities, q_s is the surface charge density, $\nabla_s = (\mathbf{I} - \mathbf{nn}) \cdot \nabla$ is the surface gradient operator, and γ is the surface tension. In the stress balance (Eq. 30f), the surface gradient of surface tension gives rise to a tangential force while surface tension on a curved surface leads to a normal force (Leal, 2007, p. 78). The viscous and electric stress tensors are

$$\mathbf{T}^m = \mu(\nabla \mathbf{v} + \nabla \mathbf{v}^T); \qquad \mathbf{T}^e = \varepsilon \mathbf{E}\mathbf{E} - \frac{1}{2} \varepsilon E^2 \mathbf{I}. \tag{31}$$

On a surface with an outward normal $\mathbf{n}$ and orthogonal tangential vectors $\mathbf{t}_1$ and $\mathbf{t}_2$, the normal and tangential Maxwell stress components are

$$\mathbf{n} \cdot \|\mathbf{T}^e \cdot \mathbf{n}\| = \frac{1}{2}\|\varepsilon(\mathbf{E} \cdot \mathbf{n})^2 - \varepsilon(\mathbf{E} \cdot \mathbf{t}_1)^2 - \varepsilon(\mathbf{E} \cdot \mathbf{t}_2)^2\|, \tag{32a}$$

$$\mathbf{t}_i \cdot \|\mathbf{T}^e \cdot \mathbf{n}\| = \|\varepsilon\mathbf{E} \cdot \mathbf{n}\|(\mathbf{E} \cdot \mathbf{t}_i). \tag{32b}$$

From Eq. 32b, we note again that neither a perfect dielectric ($q_s = 0$) nor a perfect conductor ($\mathbf{E}_t = 0$) can support a tangential Maxwell stress (Chang and Yeo, 2010).

The above set of jump conditions (Eq. 30) implies that a sharp material interface can support a surface charge density, but not a surface mass density (Melcher, 1981, p. 7.8).[2] The jump condition for surface charge density (Eq. 30c) can be further expanded as

$$\frac{\partial q_s}{\partial t} + \nabla_s \cdot (q_s \mathbf{v}_s) + q_s \mathbf{n} \cdot \mathbf{v}(\nabla_s \cdot \mathbf{n}) = -\mathbf{n} \cdot \|\sigma\mathbf{E}\|, \tag{33}$$

where the surface velocity $\mathbf{v}_s = (\mathbf{I} - \mathbf{nn}) \cdot \mathbf{v}$, and the surface curvature $\kappa = \nabla_s \cdot \mathbf{n} = 1/R_1 + 1/R_2$ where R_1 and R_2 are the principal radii of curvature of the surface, e.g. $\kappa = 2/R$ for a sphere and $1/R$ for a cylinder. The term involving the surface curvature accounts for the variation of q_s due to the dilation of the surface (Leal, 2007, p. 93). Note that unlike the surface charge convection, the bulk charge convection does not enter into the balance of surface charge density because bulk free charges never reach the interface by convection (Melcher, 1981, p. 2.18). The jump condition for surface charge density (Eq. 30c) assumes negligible surface diffusion current and surface Ohmic current, in other words, the surface convection current is assumed to dominate. Although the negligence of the surface diffusion current appears to be consistent with negligible bulk diffusion current, the negligence of the surface conduction current is not entirely justifiable from first principles. However, the simplified jump condition in the form of Eq. 30c is often sufficient to model electrohydrodynamic phenomena, see for example the literature reviewed in Saville (1997) and Zeng and Korsmeyer (2004).

2.4 Model problems of electrohydrodynamic stability

We shall now apply the governing equations of electrohydrodynamics to two model problems, electrokinetic mixing flow and electrohydrodynamic

[2] Electrical double layer is not considered here because the Ohmic model does not apply within the double layer. The inclusion of double layer may also disrupt the continuation of tangential electric fields (Melcher, 1981, p. 2.16).

cone-jet (Figure 3). Both problems are motivated by a broad range of practical applications, typically with a working fluid of relatively high conductivity ($\gtrsim 10^{-4}$ S/m) where the Ohmic model holds. Since deionized water has a conductivity of approximately 10^{-4} S/m when equilibrated with carbon dioxide in the atmosphere, the "high-conductivity" regime encompasses all practical aqueous solutions (see also discussions below around Eq. 49).

The model problems are chosen to represent two extreme scenarios. In the electrokinetic mixing flow discussed here, two *miscible* working fluids are driven by an electric field approximately *parallel* to the material interface. In contrast, in the electrohydrodynamic cone-jet, two *immiscible* working fluids are stressed by an electric field with a component *perpendicular* to the interface. We will start with the mixing flow problem where the base state is well defined, and then take on the more difficult case of cone-jet flow where a clear-cut description of the base state is a challenge in itself.

Because both model problems are open flow systems, it is useful to study the instability in the spatial frame work in addition to the more conventional temporal frame work. A system that is unstable in a temporal framework can be either convectively or absolutely unstable in the spatial framework (Huerre and Rossi, 1998; Schmid and Henningson, 2001). The onset condition of convective instability is the same as that of a temporal instability in which a global disturbance grows in time (Schmid and Henningson, 2001). Consider a disturbance introduced at a localized point in space: if it grows only downstream, the system is convectively unstable; if the disturbance grows both downstream and upstream, the system is absolutely unstable. Physically, a convectively unstable system is a noise amplifier in which a disturbance at the origin is amplified downstream, while an absolutely unstable system is an intrinsic oscillator in which the downstream propagating wave oscillates simultaneously with an upstream propagating waves (Huerre and Rossi, 1998).

3 Electrokinetic Mixing Flow

Micro total analysis systems (μTAS) aim to integrate multiple assaying functions including sample pretreatment, mixing and separation on a microfabricated chip (Manz et al., 1990; Stone et al., 2004). Electrokinetics is often the method of choice for reagent transport and manipulation in μTAS (Stone et al., 2004; Chang and Yeo, 2010). As devices gain complexity, robust control of electrokinetic processes with heterogeneous samples becomes critical. One important regime is on-chip biochemical assays with high conductivity gradients, which might occur intentionally as in sample stacking processes, or unavoidably as in multi-dimensional assays. Such conductivity

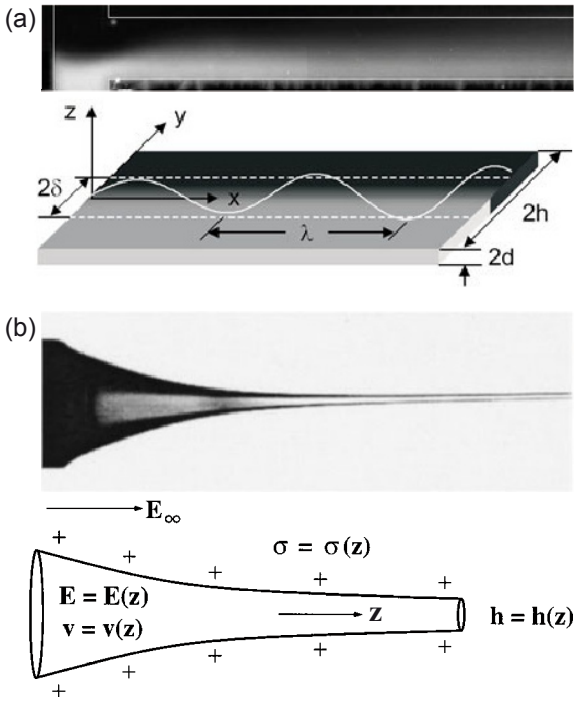

Figure 3. Model problems of electrohydrodynamic stability: (a) Electrokinetic mixing flow of two miscible streams at a T-junction. The two fluids have the same properties except for different electrical conductivities. Although the conductivity gradient leads to instability at high electric fields, the base state is the well-known diffusive solution when the material interface is approximately parallel to the applied electric field. (b) Electrohydrodynamic cone-jet with a liquid jet issued from the Taylor cone on an electrified nozzle. The inner fluid and the surrounding air have dramatically different electrical properties, with the liquid modeled as a leaky dielectric while the air as an insulator. The base state is strongly dependent on the applied electric field which has a significant component perpendicular to the material interface. A complete mechanistic understanding of the base state is not yet available. Figure (a) reprinted with permission from Chen et al. (2005), © 2005 Cambridge University Press. Figure (b) reprinted with permission from Hohman et al. (2001a,b), © 2001 American Institute of Physics.

gradients may lead to instabilities under high electric fields (Figure 4), with anecdotal evidences widespread in the μTAS literature (Chen et al., 2005). Although instability is undesirable for robust electrokinetic assay, it is useful for rapid mixing at low Reynolds number (Oddy et al., 2001). In either case, the instability mechanism must be understood before enhancement or suppression can be engineered.

As shown below, these "electrokinetic instabilities" (Lin et al., 2004; Chen et al., 2005) are fundamentally electrohydrodynamic, in which electroosmotic flow mainly acts as a convecting medium (Chen et al., 2005). The instability waves in Figure 4 clearly originate at the liquid interface with gradients of material properties, not on charged solid walls. We will also show that electroosmotic bulk flow in electrokinetic systems leads to convective and absolute instability; see Figure 4a and Figure 4b, respectively. The absolute instability sets in when the internally generated electroviscous velocity disturbances are high enough to overcome electroosmotic convection. Both the electroviscous and electroosmotic velocities result from balancing electric body forces and viscous stresses. However, the electroviscous velocity is due to the accumulated net charge density in the *bulk* (Melcher, 1981), while the electroosmotic velocity is due to the net charge within the electric double layer at the *boundary* (Chang and Yeo, 2010).

According to Eq. 27, electromechanical coupling may arise from a gradient of permittivity and/or conductivity along the electric field (Melcher, 1974). However, permittivity gradient is negligible because a dilute solution of electrolyte does not significantly alter the permittivity of pure water (Chen et al., 2005). As shown in a series of papers published by Melcher and coworkers, a sharp interface separating regions of identical properties except disparate conductivities is linearly stable (Melcher and Schwartz, 1968); however, a diffuse interface under the same condition gives rise to unstable electromechanical coupling (Hoburg and Melcher, 1976). Compared to the surface-coupled model where the electromechanical coupling is through interfacial stresses, the bulk-coupled model implies coupling through volumetric forces distributed across the diffusive interface. The diffusive interface model is particularly relevant to microsystems with small length scales, e.g. a diffusion length comparable to the channel width is visible in the unperturbed base state (Figure 3a). Consistent with the bulk-coupled model, the diffusive term should be kept in the conductivity conservation Eq. 29 (Baygents and Baldessari, 1998). Without the diffusive term, the linearized equations will be unconditionally unstable as in Hoburg and Melcher (1976), which contradicts with an experimentally measured threshold electric field below which the flow is stable (Chen et al., 2005).

The following discussions on electrokinetic mixing flow will closely follow

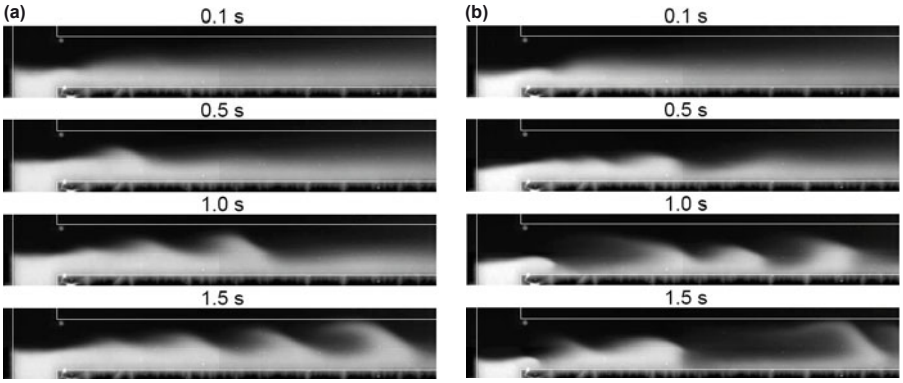

Figure 4. Instability in electrokinetic mixing flow of two miscible streams of aqueous electrolytes: (a) convective instability at a nominal external field of 1.0 kV/cm; and (b) absolute instability at 2.0 kV/cm in (b). The channel has a width of 155 μm and a depth (into the paper) of 11 μm; the conductivity ratio is $\eta = 10$ with the dyed side having the higher conductivity of $\sigma = 7.7 \times 10^{-2}$ S/m; the permittivity of both streams is $\varepsilon = 6.9 \times 10^{-10}$ C/V·m. Reprinted with permission from Chen et al. (2005), © 2005 Cambridge University Press.

Chen et al. (2005). A review of recent development in the area of electrokinetic instability can be found in Lin (2009).

3.1 Linearized thin-layer equations

The governing equations for the bulk-coupled model (Chen et al., 2005) are essentially the same as Eqs. 26 and 29. Because of the rapid charge relaxation in aqueous electrolytes, the charge conservation equations (Eq. 26c) is simplified to the continuity of Ohmic current,

$$\nabla \cdot \sigma \nabla \phi = 0, \tag{34}$$

where the quasi-electrostatic field is related the potential by $\mathbf{E} = -\nabla\phi$. The polarization term drops out of Eq. 26e because of negligible permittivity gradients.

With thin Debye length, the physics of the electric double layer is assumed to influence the instability dynamics *only* in that the double layer determines an electroosmotic velocity very close to the microchannel wall

(Chen et al., 2005). The boundary conditions at the solid walls are therefore,

$$\mathbf{n} \cdot \nabla \sigma = 0, \tag{35a}$$

$$\mathbf{n} \cdot \nabla \phi = 0, \tag{35b}$$

$$\mathbf{v} = -\varepsilon \zeta \nabla \phi / \mu, \tag{35c}$$

where $\mathbf{n}$ denotes wall-normal direction, and ζ is the zeta potential of the electrical double layer. Boundary conditions (35a) and (35b) are consequences of non-penetrating walls. The electroosmotic velocity at the wall is is given by the Smoluchowski equation (35c) (Chang and Yeo, 2010). Here, we assume constant zeta potential for simplicity. In reality, zeta potential is related to ionic concentration and therefore changes with the electrical conductivity. However, the dependence of zeta potential on local conductivity has been shown to be not essential to the instability mechanism (Chen et al., 2005).

The base state is assumed parallel, in particular, the conductivity distribution assumes a diffusive profile with a constat diffusion length δ (Figure 3a),

$$\sigma_0 = \sigma_L + \frac{\sigma_H - \sigma_L}{2} \mathrm{erfc}\left(\frac{y}{\delta}\right), \tag{36}$$

where σ_H and σ_L are respectively the high and low conductivities of the streams prior to mixing. The base electroosmotic velocity profile is assumed uniform, $U_{eo} = \varepsilon \zeta_r E_a / \mu$, where ζ_r is the reference zeta potential and E_a is the applied electric field which is assumed uniform. By the parallel base state assumption, the linear stability analysis is greatly simplified and no boundary conditions are needed in the streamwise (x-direction). The validity of the parallel base state assumption is discussed in details in Chen et al. (2005).

As mentioned earlier, two velocity scales are necessary to properly scale the governing equations in electrokinetic mixing flow. The electroosmotic velocity (U_{eo}) is the imposed velocity scale due to the net charge in the electric double layer (close to the wall), and is introduced as part of the boundary conditions. The electroviscous velocity (U_{ev}) is the internal scale for velocity disturbances due to net charge accumulation in the diffusive conductivity interface (in the bulk).

Motivated by the high-aspect ratio experimental system, we shall focus on the asymptotic thin-layer limit where $d/h \ll 1$, i.e. the channel depth ($2d$) is much thinner than the horizontal length scales which are all assumed to be on the same order of the channel width ($2h$). In the thin-layer limit, conductivity (σ) and potential (ϕ) are both independent of the z, but velocity ($\mathbf{v}$) has a z-dependence. The difference in z-dependence reflects the fact

that the walls at $z = \pm d$ prohibit mass or electric fluxes, but accommodates momentum fluxes. Therefore, the velocity profile takes the form of,

$$\mathbf{v} = \mathbf{v}_0 + \tilde{\mathbf{v}}_H = \mathbf{v}_0 + \bar{\mathbf{v}}_{ev}(x, y, t)g(z) + \bar{\mathbf{v}}_{eo}(x, y, t), \tag{37}$$

where the subscript 0 denotes the base state, the subscript H denotes the horizontal direction, g(z) is a parabolic function $g(z) = \frac{3}{2}(1 - z^2/d^2)$, $\bar{\mathbf{v}}_{ev}$ and $\bar{\mathbf{v}}_{eo}$ are the electroviscous and electroosmotic velocity perturbation with the over bar denoting a depth-averaged quantity, and the electroosmotic velocity perturbation is given by

$$\bar{\mathbf{v}}_{eo} = -U_{eo}\left(\frac{\partial_x \bar{\phi}}{E_a}\boldsymbol{e}_x + \frac{\partial_y \bar{\phi}}{E_a}\boldsymbol{e}_y\right). \tag{38}$$

After depth averaging, the linearized conductivity conservation and momentum equations take the form of

$$\frac{\partial \bar{\sigma}}{\partial t} + \mathbf{v}_0 \cdot \nabla_H \bar{\sigma} + \bar{\mathbf{v}} \cdot \nabla_H \sigma_0 = {\nabla_H}^2 \bar{\sigma}, \tag{39}$$

$$\rho\frac{\partial \bar{\mathbf{v}}}{\partial t} + \rho(\mathbf{v}_0 \cdot \nabla_H)\bar{\mathbf{v}} + \rho(\bar{\mathbf{v}} \cdot \nabla_H)\mathbf{v}_0 = -\nabla_H \bar{p} + \mu {\nabla_H}^2 \bar{\mathbf{v}} - \frac{3\mu}{d^2}(\bar{\mathbf{v}} - \bar{\mathbf{v}}_{eo}) + \bar{\rho}_f \boldsymbol{E}_0, \tag{40}$$

where $\boldsymbol{E}_0 = E_a \boldsymbol{e}_x$. The form of mass continuity and current continuity equations remains essentially unchanged. See Chen et al. (2005) for an asymptotic derivation of the thin-layer equations.

Balancing the viscous and electric forces in the linearized momentum Eq. 40, the electroviscous velocity can be shown to scale as (Chen et al., 2005),

$$U_{ev} \sim \frac{\bar{\rho}_f E_a}{\mu/d^2} \sim \frac{(\eta - 1)^2}{(\eta + 1)^2}\frac{d^2}{\delta}\frac{\varepsilon E_a^2}{\mu}. \tag{41}$$

Note δ is the diffusion half length across which conductivity varies, and is therefore the relevant length scale for charge density. However, d is the relevant length scale for wall-bounded viscous transport. The terms involving $\eta = \sigma_H/\sigma_L$ account for the conductivity gradient. This definition of U_{ev} strives to account for all the relevant physical parameters involved in the electroviscous balance of the problem. Fundamentally, Eq. 41 is the same as the simpler version in Hoburg and Melcher (1976) and Melcher (1981), both containing the electroviscous time scale of $\mu/\varepsilon E_a^2$. Note that U_{ev} scales as E_a^2 while U_{eo} scales as E_a, because the electroviscous velocity results from induced charge density which itself scales as E_a.

In modeling electrokinetic instabilities, it is important to note that U_{eo} is the velocity scale for the base electroosmotic flow, while U_{ev} is the internally

generated velocity scale to properly scale the perturbation velocity. With proper nondimensionalization, two governing parameters naturally appears in the conductivity conservation Eq. 39,

$$\frac{1}{R_v}\left(\partial_T\bar{\Sigma}+U_0\partial_X\bar{\Sigma}\right)+(\partial_Y\Sigma_0)\bar{V}=\frac{1}{Ra_e}\nabla_H^2\bar{\Sigma}, \tag{42}$$

where capital letters denote nondimensional variables (except E which does not appear in the nondimensional equations), i.e. a general field variable Λ is decomposed in nondimensional form as $\Lambda=\Lambda_0+\bar{\Lambda}$. The electroviscous-to-electroosmotic velocity ratio R_v is defined as

$$R_v=\frac{U_{ev}}{U_{eo}}=\frac{(\eta-1)^2}{(\eta+1)^2}\frac{E_a d^2}{\zeta_r\delta}. \tag{43}$$

The electric Rayleigh number Ra_e is defined as

$$Ra_e=\frac{U_{ev}h}{D_{eff}}=\frac{(\eta-1)^2}{(\eta+1)^2}\frac{h}{\delta}\frac{\varepsilon E_a^2 d^2}{\mu D_{eff}}, \tag{44}$$

which measures the relative importance of dynamic (electric body) forces to dissipative forces by molecular and viscous diffusion.

3.2 Results of linear stability analysis

The instability mechanism is evident from the most unstable eigenmodes of a representative convective instability shown in Figure 5 (Hoburg and Melcher, 1976; Chen et al., 2005). Figure 5a: The eigenmode of conductivity perturbation has a cellular pattern and alternates in sign in the x-direction. Figure 5b: Such conductivity perturbation will change the electric potential distribution due to current continuity (see also Figure 5e). Figure 5c: The perturbed electric field will produce a charge density perturbation by Gauss's Law, and leads to electric body forces. Figure 5d: The electric body forces produce cellular fluid motion through the Navier-Stokes equations. This fluid motion further alters the conductivity field through the convection-diffusion equation of conductivity, and the positive feedback leads to instability. The similarity of perturbation patterns of the stream function ($\bar{\Psi}$) and y-direction gradient of electric potential ($\bar{\Phi}$), shown by Figure 5d and Figure 5e, confirms a useful relationship in the absence of electroosmotic flow (Chen et al., 2005),

$$\bar{\Psi}\propto\partial_Y\bar{\Phi}. \tag{45}$$

The analytical expression (Eq. 45) directly relates the electric and velocity fields, which enables us to explain the instability mechanism in a

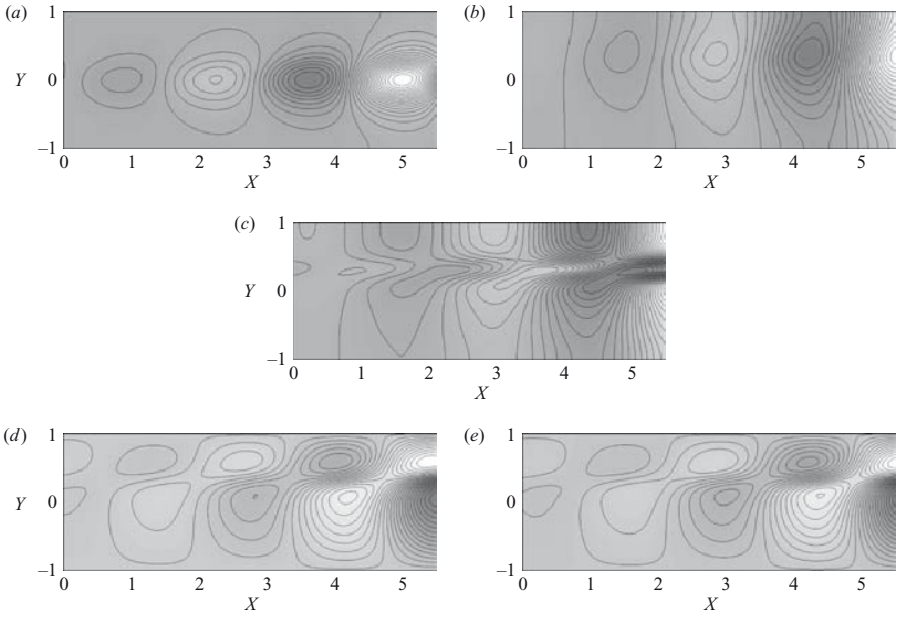

Figure 5. Electrokinetic instability mechanism shown by the most unstable eigenmodes. Dark gray is negative and light gray is positive, contour plots are overlayed: (a) $\bar{\Sigma}$, conductivity perturbation; (b) $\bar{\Phi}$, potential perturbation; (c) $\nabla_H^2 \bar{\Phi}$, which is proportional to negative charge density; (d) $\bar{\Psi}$, streamfunction perturbation; (e) $\partial_Y \bar{\Phi}$, electric field perturbation. Conductivity perturbation alternates electric potential distribution and induces bulk charge accumulation, which in turn results in electric body forces and promotes cellular fluid motion. The cellular flow further perturbs the conductivity field and this positive feedback leads to instability. Reprinted with permission from Chen et al. (2005), © 2005 Cambridge University Press.

more intuitive way (Figure 6) (Chen et al., 2005). When the initially flat interface is perturbed, the perturbed conductivity field will alter the electric field. The local electric field is strengthened where lower conductivity replaces higher conductivity (region II), and vice versa (region I). The electric field perturbation is strongest at the conductivity interface (dot-dashed line) and decays away from it. According to Eq. 45, the velocity perturbation further stretches the interface upward for regions I and downward for regions II. This tendency for the perturbed interface to be further stretched is competing with molecular diffusion. When the electroviscous process is faster than molecular diffusion, i.e.

$$\frac{h}{U_{ev}} < \frac{h^2}{D_{eff}} \quad \Rightarrow \quad Ra_e > 1, \tag{46}$$

the perturbation at interface will grow and lead to instability.

In the presence of electroosmotic flow, the unstable perturbations grow as they are convected downstream, which leads to convective instability if the disturbance is not too strong. In the regime of convective instability, growth rate is finite at any downstream location and the regions upstream of the initial disturbance are largely unaffected. However, when the internal electroviscous process is faster than the external electroosmotic convection, i.e.

$$\frac{h}{U_{ev}} < \frac{h}{U_{eo}} \quad \Rightarrow \quad R_v > 1, \tag{47}$$

the flow may become absolutely unstable because the electroosmotic flow can not carry the disturbances downstream fast enough. Therefore, in the regime of absolute instability, the disturbance grows in time (t) at the origin and the upstream flow is perturbed.

The above heuristic arguments are confirmed by the linear stability analysis (Chen et al., 2005). All seven nondimensional parameters in the problem are systematically varied, some over three orders of magnitude. The critical conditions for convective and absolute instabilities are plotted on a $Ra_e - R_v$ phase diagram (Figure 7). It is obvious from the figure that the onset of convective instability collapses around $Ra_{e,cr} \simeq 10$, while the onset of absolute instability collapses around $R_{v,cr} \simeq 4$. When the system properties are fixed, the electric Rayleigh number and the electroviscous-to-electroosmotic velocity ratio vary along a fixed curve $Ra_e \propto R_v^2$. As electric field is increased, the system first become convectively unstable when Rayleigh number exceeds $Ra_{e,cr}$, and then absolutely unstable when the velocity ratio exceeds $R_{v,cr}$.

Despite the linearization with depth averaging and parallel base state, the above model agrees reasonably well with experiments (Chen et al., 2005).

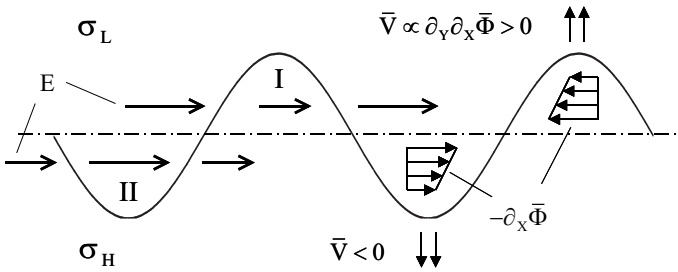

Figure 6. Schematic of electrohydrodynamic instability mechanism. When the conductivity interface is perturbed, the electric field is perturbed due to alternation of conductivity. The perturbed electric field is strongest at the conductivity interface (dot-dashed line) and decays away from it, this gradient in electric field results in vertical velocities which further stretch the interface. Reprinted with permission from Chen et al. (2005), © 2005 Cambridge University Press.

The model captures trends of the instability as a function of increasing field strength, and predicts the observable quantities such as spatial growth rates within a factor of three. Take the critical electric field for example, the nominal threshold for onset of (convective) instability was 0.5 ± 0.1 kV/cm in experiments, and is 0.14 kV/cm from the linear stability analysis; The onset of absolute instability was about 1.5 kV/cm in experiments (Figure 4), and is 0.65 kV/cm from the analysis. With slight modifications, the model also predicts the onset of convective instability in a different geometry where three liquid streams mix at a cross-junction (Posner and Santiago, 2006).

The model presented here offers a useful framework to address the stability issues of electrokinetic mixing flow. We emphasize again that the electrokinetic flow instability resulting from electrical conductivity gradients is essentially an electrohydrodynamic instability convected by the electroosmotic flow. To suppress instability in electrokinetic assays, one needs to minimize Ra_e, the ratio of dynamic electric body forces to dissipative forces due to molecular and viscous diffusion, which controls the onset of instability. To enhance instability for microfluidic mixing, one needs to maximize R_v, the ratio of internally generated electroviscous velocity to bulk electroosmotic velocity, which controls the absolute verses convective nature of instability.

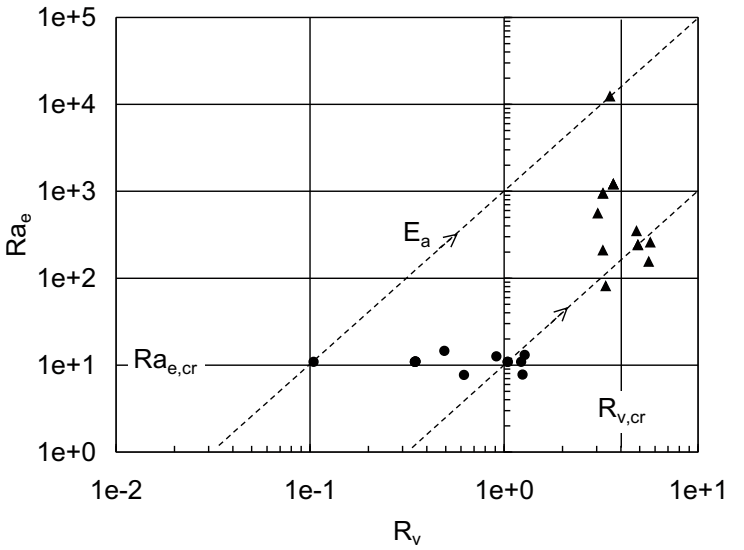

Figure 7. Phase diagram for convective and absolute instability. The critical conditions are plotted with circles representing onset of convective instability and triangles absolute instability. At onset of convective instability, the critical Rayleigh number collapses around $Ra_{e,cr} \simeq 10$. At onset of absolute instability, the critical velocity ratio collapses around $R_{v,cr} \simeq 4$. Note that at a given condition, Ra_e/R_v^2 is a constant so Ra_e and R_v can not be independently varied. Reprinted with permission from Chen et al. (2005), © 2005 Cambridge University Press.

4 Electrohydrodynamic cone-jet

Electrohydrodynamic cone-jet transition is a unique phenomenon that permits the production of a tiny liquid jet from a much larger nozzle (Cloupeau and Prunet-Foch, 1989; Fernandez de la Mora, 2007). The large drawdown ratio enables a variety of techniques including electrospraying, electrospinning and electrostatic printing (Figure 8). Electrospraying has a broad spectrum of applications, most notably crop and paint spraying and electrospray ionization (Bailey, 1988; Kebarle and Verkerk, 2009). Electrospinning is mainly used in producing nanoscale fibers and miniaturized encapsulation (Reneker et al., 2007; Barrero and Loscertales, 2007). Electrostatic printing is useful for high-resolution production of biomolecular microar-

rays and electronic circuits (Yogi et al., 2001; Park et al., 2007). The stability of electrohydrodynamic cone-jet is of paramount importance to its practical applications. Electrospraying and electrospinning hinges on the *downstream* destabilization of a steady cone-jet to generate fine droplets or thin fibers (Fernandez de la Mora and Loscertales, 1994; Hohman et al., 2001a), while electroprinting relies on transient cone-jets to deploy drops on demand (Chen et al., 2006a,b).

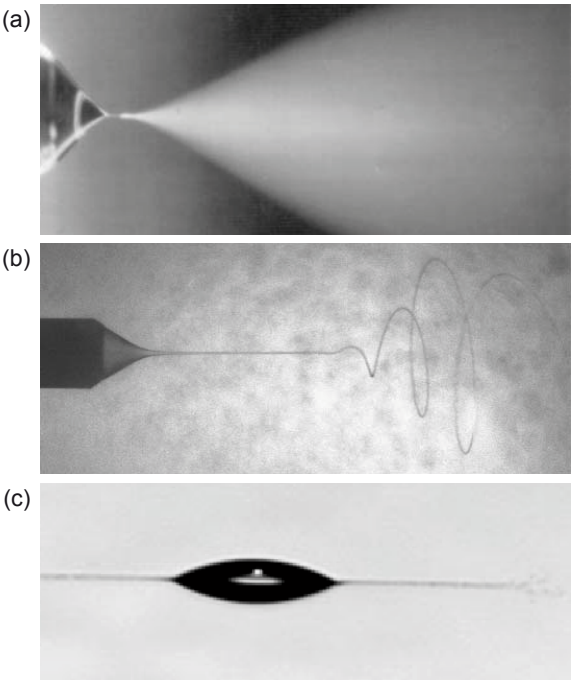

Figure 8. Electrohydrodynamic cone-jets in the context of (a) electrospraying, (b) electrospinning, and (c) electrostatic explosion. Unlike the steady cone-jet in (a) and (b), the cone-jet in (c) is inherently transient, similar to the transient jetting process in electrostatic printing. Figures (a) and (b) reprinted with permission from Barrero and Loscertales (2007), © 2007 Annual Reviews. Figure (c) reprinted with permission from Duft et al. (2003), © 2003 Nature Publishing Group.

In contrast to its wide-ranging applications, a complete mechanistic understanding of the cone-jet dynamics remains elusive. In addition to the mathematical complexities in analyzing multi-physical free surface flow, ex-

perimental measurements are also difficult for the flow fields in a free jet, the diameter of which is often on the verge of optical resolution. For a summary of the state-of-the-art and a discussion of unresolved issues, see Fernandez de la Mora (2007); Barrero and Loscertales (2007); Ganan-Calvo and Montanero (2009). The incomplete understanding of the steady cone-jet significantly complicates the stability analysis which needs a base state to start with.

In this section, we will first discuss the operating regime of a steady cone-jet, and then discuss a few selected papers on the cone-jet stability. The dynamics of the electrified jet will be compared to its uncharged counterpart (Eggers and Villermaux, 2008). Because there is a well-defined interfacial boundary between the liquid jet and its immiscible surrounding fluid (e.g. air), a surface-coupled model will be adopted as in the study of conventional uncharged jets.

4.1 Operating diagram of a steady cone-jet

Steady cone-jet is the most useful of the many possible functioning modes of an electrified meniscus (Cloupeau and Prunet-Foch, 1989; Fernandez de la Mora, 2007). For a given working fluid, the conditions leading to steady cone-jet are best summarized by the stability island in the $E - Q$ operating diagram (Figure 9), which is obtained by independently varying the externally applied parameters of electric field (E) and flow rate (Q). The detailed shape of the stability island varies among different working fluids and different electrode configuration. The stability boundary also exhibits a fairly pronounced hysteresis (Cloupeau and Prunet-Foch, 1989; Fernandez de la Mora, 2007). Fortunately, the minimum flow rate (Q_m) and the associated electric field (E_m) in Figure 9 can be rationalized as follows.

When a liquid meniscus is electrified, the Maxwell stress leads to interfacial deformation. At a sufficiently high electric field, the meniscus takes the shape of a Taylor cone (Taylor, 1964). Balancing the electric stress and surface tension, the critical electric field scales as (Taylor, 1964; Smith, 1986)

$$E_m \sim \sqrt{\frac{\gamma}{\varepsilon_0 a}}, \tag{48}$$

where a is a characteristic length scale such as the radius of the nozzle to which the meniscus attaches.[3] For a perfectly conducting liquid, the cone surface is equipotential with a theoretical half angle of 49.3° (Taylor, 1964). See Fernandez de la Mora (2007) for a discussion of other possible conical configurations.

[3]Some operating diagrams use voltage as the control variable. For the commonly used

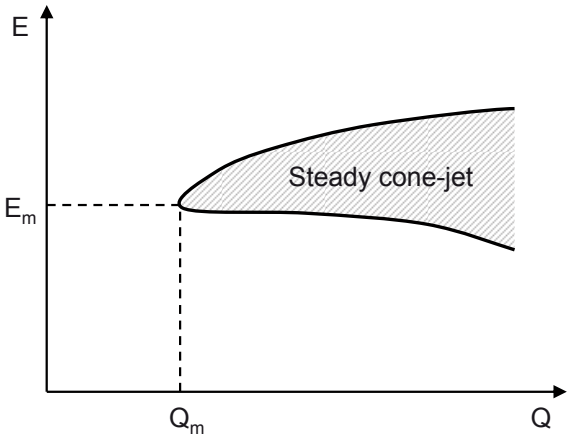

Figure 9. Operating regime of steady cone-jet: At the minimum flow rate Q_m, the applied electric field should be E_m to produce a stead cone-jet; Above Q_m, a steady cone-jet can be produced in a limited range of electric field around E_m; Below Q_m, a steady cone-jet is not possible but pulsating cone-jet results around E_m.

For a relatively conducting liquid, the minimum flow rate does not depend on viscosity (the jet has an approximately flat velocity profile); On dimensional ground Q_m scales as (Fernandez de la Mora and Loscertales, 1994; Fernandez de la Mora, 1996),

$$Q_m \sim \frac{\gamma\varepsilon}{\rho\sigma}. \tag{49}$$

This scaling law is empirically known to work in the "high-conductivity" limit with $\sigma \gtrsim 10^{-4}$ S/m, but a rigorous theoretical justification is still missing (Fernandez de la Mora, 2007). Higher conductivities usually lead to finer sprays, but for conductivities higher than 1 S/m, direct ion evaporation may be possible (Fernandez de la Mora, 2007). Many electrospray working fluids (including most aqueous solutions) are within this intermediate conductivity regime between 10^{-4} and 1 S/m.

needle-to-plate configuration, the critical voltage can be approximated as

$$\Phi_m \approx E_m a \sqrt{\frac{\cos\theta}{2}} \ln\left(\frac{4l}{a}\right),$$

where θ is the conical half angle. This expression is valid when the electrode separation (l) is much larger than the needle radius (a) (Smith, 1986; Kebarle and Verkerk, 2009).

The dynamics outside of the steady cone-jet regime is very poorly understood, see for example Cloupeau and Prunet-Foch (1994); Grace and Marijnissen (1994). With the caveats of being overly simplified and *incomplete*, a sketch of the operating modes in the $E-Q$ diagram is offered as follows:

- $Q < Q_m$: If the flow rate is smaller than the theoretical minimum, a stable jet is not possible and a variety of pulsating modes may result.
  $E \simeq E_m$**:** *Pulsating cone-jet*, which results from the imbalance of supplied and jetted flow rates. Many electrostatic printing and "nanoelectrospray" (Wilm and Mann, 1994) systems fall in this pulsating regime as a result of the increased drag in miniaturized nozzles. The pulsation mechanism will be discussed below.
- $Q \gtrsim Q_m$: If the flow rate is intermediate for which a steady cone-jet is possible, the mode of operation depends strongly on the electric field:
  $E \ll E_m$**:** *Dripping*, which is analogous to hydrodynamic dripping (Eggers and Villermaux, 2008).
  $E \lesssim E_m$**:** *Pulsating cone-jet*, which sometimes resembles the aforementioned case when $Q \lesssim Q_m, E \simeq E_m$. This transition region is very complex and can be subdivided further into bursting, pulsating and astable modes, where the astable mode is not periodic at all (Marginean et al., 2007).
  $E \simeq E_m$**:** *Cone-jet*, which is the most useful mode (Fernandez de la Mora, 2007) and the benchmark that all other operating modes are compared against. Electrospraying and electrospinning systems typically employ a stable cone-jet, which eventually destabilizes downstream in the *varicose* or *kink* (whipping) mode, respectively. The instability mechanism will be discussed below.
  $E \gg E_m$**:** *Multi-jet*, which occurs when the rapidly accumulated surface charges must be redistributed through multiple jets. There are many other possible modes in addition to the multi-jet one (Cloupeau and Prunet-Foch, 1994), but these highly unstable modes are rarely used in practice.
- $Q \gg Q_m$: If the flow rate is much larger than the theoretical minimum, a hydrodynamic jet results instead of a cone-jet; this hydrodynamic regime is usually not of practical interest (Grace and Marijnissen, 1994).

4.2 Long-wavelength model

Consistent with the surface-coupled model adopted below, the working fluid is assumed to be a leaky dielectric such that (i) the liquid is sufficiently

conducting to carry electric charges only on its surface and any bulk charge will instantaneously relax to the interface; (ii) the liquid is sufficiently dielectric to support a tangential electric field (Melcher and Taylor, 1969; Melcher and Warren, 1971; Ganan-Calvo, 1997a; Hohman et al., 2001a; Feng, 2002). Note that the assumption of instantaneous charge relaxation refers to the *local* relaxation of bulk charge density (Ganan-Calvo, 1997a; Hohman et al., 2001a). The external fluid (air) is assumed to have no effect on the jet except to provide a uniform external pressure. As we have stressed earlier, only a leaky dielectric can support tangential shear stress, which pulls charge and mass toward the conical tip and is the root cause for the eventual jet issuance (Hayati et al., 1986); cf. Figure 2c. We shall restrict our discussions to Newtonian fluids; for non-Newtonian effects, see for example Reneker et al. (2007); Feng (2002).

In the long-wavelength limit, the electrified jet is asymptotically governed by a set of one-dimensional equations (Hohman et al., 2001a; Feng, 2002). In the axisymmetric case,

$$\partial_t(\pi h^2) + \partial_z(\pi h^2 v) = 0, \tag{50a}$$

$$\partial_t(2\pi h q_s) + \partial_z(2\pi h q_s v + \pi h^2 \sigma E) = 0, \tag{50b}$$

$$\rho(\partial_t v + v\partial_z v) = -\partial_z p_{tot} + \rho g + \frac{2}{h} q_s E + \frac{3}{h^2}\mu\partial_z(h^2\partial_z v), \tag{50c}$$

with

$$p_{tot} = \gamma\kappa - \frac{1}{2}(\varepsilon - \varepsilon_0)E^2 - \frac{q_s^2}{2\varepsilon_0},$$

and

$$E = E_\infty + \ln\xi\left[\frac{1}{\varepsilon_0}\partial_z(q_s h) - \frac{\varepsilon - \varepsilon_0}{2\varepsilon_0}\partial_z^2(Eh^2)\right], \tag{50d}$$

where $h(z)$ is the jet radius, v and E are the velocity and electric field in the axial z-direction, E_∞ is the external field in the absence of the jet, ξ is the local aspect ratio assumed to be small; for the linearized system, ξ is proportional to the wave number (Hohman et al., 2001a). Eq. 50a is the conservation of mass. Eq. 50b is the conservation of current, where the jet current consists of both surface convection and bulk conduction. The momentum Eq. 50c incorporates the same hydrodynamic terms as nonelectrical jets (Eggers and Villermaux, 2008) and a few additional electrical terms: the $q_s E$ term is related to the tangential electrical force (cf. Figure 2c), $(\varepsilon-\varepsilon_0)E^2/2$ is the polarization force under an external field (cf. Figure 2b), and $q_s^2/2\varepsilon_0$ is the radial repulsion of surface charge (cf. Figure 2a). Eq. 50d approximates the electrostatic field inducted by the surface charge by an effective line charge along the axis; for alternative approximations,

see e.g. Ganan-Calvo (1997a). The key notion is that the self-inducted field modifies the imposed electric field, which complicates the coupled dynamics between electric and flow fields. Note that Eq. 50 is asymptotically valid for a slender jet in the long-wavelength limit with an additional requirement unique to electrified jet: the tangential electric stress must be much smaller than the radial viscous stress, $q_s E \ll \mu v/h$ (Hohman et al., 2001a).

The long-wavelength limit represents a major simplification to the governing equations while keeping the essential physics. The governing equations suitable for a whipping jet with curved centerline have also been derived in Hohman et al. (2001a). Among other complications, the bending introduces nonaxisymmetric distortions which necessitates the introduction of dipole in addition to monopole charge density. In the interest of space, we will base our discussions on the axisymmetric equations (Eq. 50), which contains the majority of the physics; however, we will cite results from the full governing equations applicable to both varicose and whipping instabilities.

Before discussing the electrified jet, it is instructive to review the stability physics of a purely mechanical jet. In a nonelectrical jet, surface tension is destabilizing and drives the well-known varicose instability first analyzed by Rayleigh (1879). The instability mechanism is that the perturbed jet gives rise to a lower overall surface energy when the wavelength is longer than the perimeter of the jet. All azimuthal modes are stable as surface corrugation always carries a penalty in surface energy. Both longitudinal stretching and viscous stresses slow down the instability and increases the most amplified wavelength. More details on nonelectrical jet can be found in Eggers and Villermaux (2008).

In an electrified jet, three additional terms are in action at the interface:[4] the normal polarization force due to the permittivity gradient at the liquid/air interface, the normal Coulombic force due to *self*-repulsion of the free surface charge, and the tangential electric stress on the free surface charge. Their roles in electrohydrodynamic stability are summarized as follows:

- The polarization forces is stabilizing in a current-carrying jet. A local constriction of the jet increases the electric field (by current conservation) which increases the outward polarization force to resist the constriction (Melcher and Warren, 1971).
- The self repulsion of surface charges stabilizes the nonelectrical varicose mode by reducing the effective surface tension, but at the same time promotes an electrical whipping mode by Coulombic repulsion

[4]The Korteweg-Helmholtz force concept is adopted, as usual, which nicely confines the polarization forces on the interfaces where there is a nonzero $\nabla\varepsilon$.

(Hohman et al., 2001a). Contrary to surface energy, electrostatic energy shrinks with expanding surface area. Nonaxisymmetric surface corrugation is therefore energetically favorable as far as electrostatic energy is concerned.

- The tangential electric stress provides a stabilizing longitudinal stretching by accelerating the jet. However, the same tangential electric stress can also destabilize the jet by promoting out-of-phase oscillation between surface charge rearrangement and the fluid response (Hohman et al., 2001a); see also discussions of Figure 12 below.

Both tangential shear stress and self repulsion can be important in promoting instability, depending on the relative magnitude of the imposed tangential electric field and the normal field induced by surface charge (Hohman et al., 2001a); see also discussions around Eq. 56 below.

The linear stability analysis by Hohman et al. (2001a) showed three instability modes: the axisymmetric Raleigh mode (the conventional varicose instability modified by the electric field), the axisymmetric conducting mode (caused by the redistribution of surface charges under an external field), and the whipping conducting mode (cf. Figure 8b). The latter two are called "conducting modes" because they only exist with a finite conductivity. The demarcation between the varicose and kink modes follows the following scaling,

$$q_{s,cr} \sim \sqrt{\frac{2\varepsilon_0\gamma}{h}}, \tag{51}$$

where the critical surface charge density ($q_{s,cr}$) is typically an order of magnitude smaller than the Rayleigh limit for electrostatic explosion (Rayleigh, 1882). The Rayleigh limit ($\sqrt{2\varepsilon_0\gamma/h}$ for a jet with a radius of h) represents the competition between electrostatic repulsion and surface tension.

To quantitative compare the simplified 1D model with experimental results, the axial distribution of the jet diameter and surface charge density were calculated by fitting the experimentally measured profile of a stable cone-jet as it thins down from the nozzle (Hohman et al., 2001b); for alternatively approaches, see the discussions in Feng (2002). The operating diagram of an electrified jet of aqueous polymer is shown in Figure 10. Remarkably, the experimentally measured operating diagram of steady cone-jet is qualitatively reproduced by the stability analysis. The lower stability boundary demarcates the varicose instability and the steady jet, and the upper one demarcates the steady jet and the whipping instability. The linear stability analysis showed that both viscosity and surface charge are important to capture the long-wavelength and whipping features of the instability, respectively (Hohman et al., 2001a). These observations are consistent with the role of viscosity in mechanical jet instability and the fact that self-

repulsive surface charge tends to maximize surface area. The model also captured scaling trends predicted by Eq. 49, with a higher conductivity leading to lower minimum flow rate (Hohman et al., 2001b). However, it should be noted that the theoretically predicted minimum flow rate based on the linear stability analysis seems to be a few orders of magnitude higher than the experimentally measured one (Figure 10).

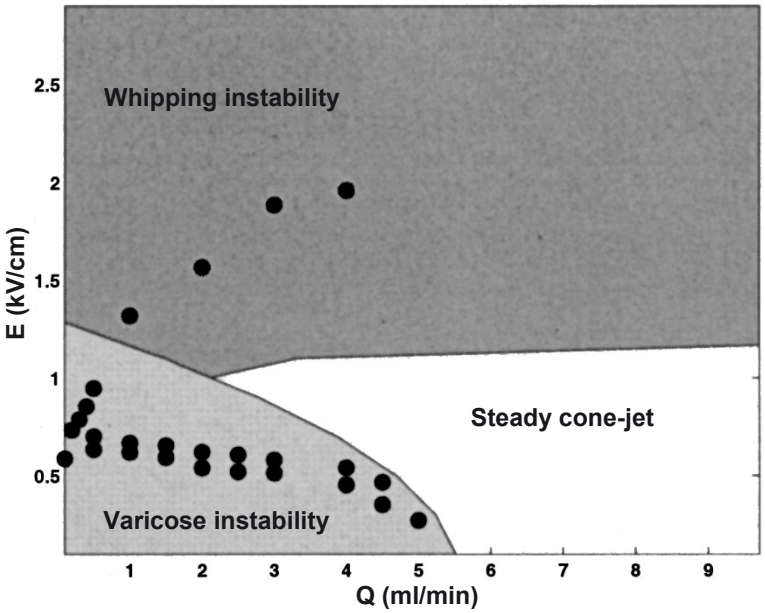

Figure 10. Prediction of varicose and whipping instabilities of an electrohydrodynamic jet using the one-dimensional model. Experimental measurements denoted by dots are overlayed on the numerical prediction with the white region denoting stable jet, light gray varicose instability, and dark gray whipping instability. The working fluid is aqueous solution of polyethylene oxide (assumed Newtonian), with $\sigma = 1.2 \times 10^{-2}$ S/m, $\varepsilon = 3.8 \times 10^{-10}$ C/V·m, $\mu = 1.7$ Pa·s, $\rho = 1.2 \times 10^3$ kg/m^3, and $\gamma = 6.4 \times 10^{-2}$ N/m. Reprinted with permission from Hohman et al. (2001b), © 2001 American Institute of Physics.

4.3 Convective and absolute instability

The convective and absolute instability transition in a charge liquid jet is studied by Lopez-Herrera et al. (2010) using a two-dimensional model of leaky dielectric jets assuming axisymmetric perturbations and negligible gravity and tangential electric field.[5] The assumption of negligible tangential electric field is relevant on a *developed* electrohydrodynamic jet where the electric current is dominated by surface convection instead of bulk conduction, and the tangential field is (typically) much smaller than the radial one induced by the free surface charge (Ganan-Calvo, 1997a,b). In this limit, the governing electrical parameters are the relative permittivity β, the relaxation parameter α, and the charge parameter χ,

$$\beta = \frac{\varepsilon}{\varepsilon_0}, \quad \alpha = \sqrt{\frac{\rho h^3 \sigma^2}{\gamma \epsilon^2}}, \quad \chi = \frac{h q_s^2}{\gamma \varepsilon_0}, \tag{52}$$

where α compares the capillary-inertial time with the charge relaxation time and χ compares the electrostatic pressure to capillary pressure. Close to the onset conditions for a stable cone-jet, calculations in Lopez-Herrera et al. (2010) showed that most cone-jet systems are moderately charged with a charge parameter χ below 1 ($\chi = 2$ at the Rayleigh limit given by Eq. 51).

For cone-jets with moderate charge parameter (χ), the absolute to convective instability (dripping to jetting) transition is found to be insensitive to electrical parameters; Instead, the transition on moderately charged jets is mainly governed by the mechanical parameters (Lopez-Herrera et al., 2010). The Weber number (We) is related to the Reynolds (Re) and Capillary (Ca) numbers by

$$We = \frac{\rho U^2 h}{\gamma} = \frac{\rho U h}{\mu} \frac{\mu U}{\gamma} = Re \cdot Ca, \tag{53}$$

The Weber number be viewed as the ratio of the imposed flow velocity (U) to the intrinsic capillary-inertial velocity ($\sqrt{\gamma/\rho h}$), similar to $1/R_v$ which is equal to the imposed electroosmotic flow to the intrinsic electroviscous velocity. Note that the Reynolds and Capillary numbers are related by the

[5] Within the limit of negligible tangential electric field, Lopez-Herrera et al. (2005) compared the more general two-dimensional model against the one-dimensional long-wavelength description, and showed that the long-wavelength limit breaks down for low-viscosity, low-conductivity/permittivity liquid. However, the long-wavelength model is usually valid for aqueous solutions due to their large conductivity and permittivity. See Lopez-Herrera et al. (2005) for details.

Ohnesorge number,

$$Oh = \frac{\mu}{\sqrt{\rho\gamma h}} = \sqrt{\frac{Ca}{Re}}, \tag{54}$$

which is not a function of velocity. Heuristically, with increasing convection velocity U, the flow transits from absolute to convective instability as the external convection process outcompetes the intrinsic capillary waves, i.e.

$$\frac{h}{U} < \frac{h}{\sqrt{\gamma/\rho h}} \quad \Rightarrow \quad We > 1. \tag{55}$$

The heuristical argument of the critical Weber number is confirmed by the spatiotemporal analysis in Figure 11, where the theoretical results are plotted along with experimental values of Reynolds and Capillary numbers for dozens of stable cone-jet configurations in the context of both electrospraying and electrospinning. The experimental conditions for stable cone-jets more or less follow a line of constant Weber number. Note that this hydrodynamically dominated criterion of stability transition breaks down in the limit of low Reynolds number, where the stability behavior is strongly sensitive to the electrical parameters (Lopez-Herrera et al., 2010).

The assumption of negligible tangential electric field is invalid close to the "neck" region of the cone-jet, where the dominant charge transport mechanism transits from bulk conduction to surface convection (Ganan-Calvo, 1997b; Lopez-Herrera et al., 2010). In the neck region, the tangential electrical stress is crucial to the dynamics of the cone-jet.

The essential role of tangential electric stress is illustrated by Figure 12 (Melcher and Warren, 1971); see also the film by Melcher (1974). The polarity of the free charge on the jet surface is controlled by a stack of wall electrodes (horizontal lines in the figure). The induced surface charge takes positive or negative polarity, depending on the relative potential between the wall electrodes and their corresponding location on the jet. The resulting tangential electric stress is either along (Figure 12a) or opposite to (12b) the jet flow direction, leading to "supercritical" and "subcritical" flow, respectively. The 1D model employed by Melcher (1974) is essentially the same as Eq. 50, with the viscous stresses and surface charge convection neglected and Eq. 50d replaced by a much simpler induction relationship. The neglection of viscous stresses reduces the system into a set of first order wave equations with upstream and downstream wave velocities a_- and a_+ *in the convective frame* traveling with the jet. In a supercritical flow represented by Figure 12a, the jet velocity exceeds the upstream wave velocity ($v > a_-$) so that downstream disturbances can not propagate upstream; In a subcritical flow ($v < a_-$) represented by Figure 12b, disturbances can

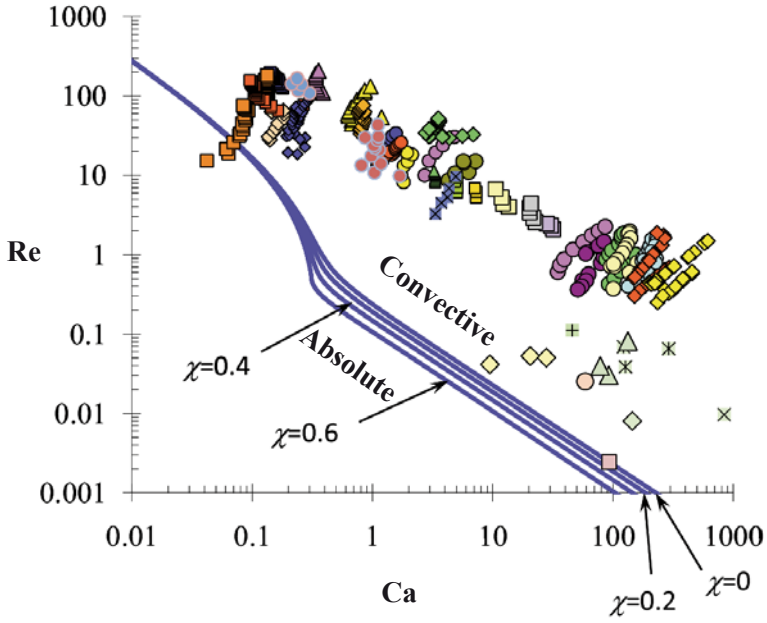

Figure 11. Absolute to convective instability transition for cone-jets. Solid curves correspond to the theoretical predictions of the critical condition as a function of the charge parameter χ (Eq. 52), while discrete data points are the Reynolds and Capillary numbers estimated from cone-jets reported in both electrospraying and electrospinning literature. Reprinted with permission from Lopez-Herrera et al. (2010), © 2010 American Institute of Physics.

propagate in both directions so the flow is dependent on both upstream and downstream conditions (Melcher and Warren, 1971). In this sense, the subcritical/supercritical jet flow is analogous to subsonic/supersonic flow of compressible gas.

The supercritical concept was originally developed to explain the unusually stable electrohydrodynamic jets with much longer breakup length compared to their nonelectrical counterparts (Melcher and Warren, 1971). Ganan-Calvo (1997a) extended this line of work to include the convection of surface charge and more importantly, self-induction of electric fields from the free surface charges (using a approach different from Eq. 50d). In Melcher (1974), the entire jet is either subcritical or supercritical when the surface charge is induced by wall electrodes. Ganan-Calvo (1997a) showed that a

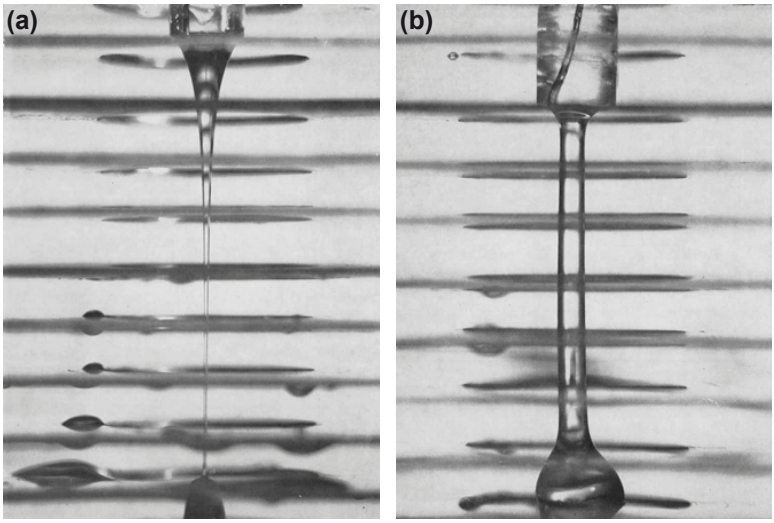

Figure 12. Reversal of the tangential electric stress on the jet leads to the transition from (a) supercritical to (b) subcritical flow. Voltage is applied between a nozzle at the top and a counter electrode at the bottom. Horizontal lines are the wall electrodes with a linear voltage dependence that is separately conrolled. In (a), dripping glycerin is accelerated into a jet by the applied electric field; In (b), the polarity of surface charge on the jet is reversed by changing the wall potentials relative to the potential on the jet; the reversed tangential electric stress leads to a subcritical flow that approaches the critical ("sonic") point at the bottom electrode. Reprinted with permission from Melcher and Warren (1971), © 1971 Cambridge University Press.

self-inductive cone-jet transits from the subcritical to supercritical regime at a critical point along the cone-jet. Downstream of the critical point, the supercritical jet eventually develops a convective instability. The supercritical portion of the jet between the critical point and the point of instability provides a shield to prevent perturbations (e.g. from jet breakup) from propagating upstream, giving rise to the unusual stability of electrohydrodynamic jets. Lopez-Herrera et al. (2010) confirmed that the jet issued from a Taylor cone is supercritical at the region prior to breakup.

In a global analysis of the cone-jet, the relative importance of the radial

to tangential electric stress,

$$\vartheta = \frac{T^e_{rr}}{T^e_{rz}} \sim \frac{q_s^2/\varepsilon_0}{q_s E_\infty} = \frac{q_s/\varepsilon_0}{E_\infty}, \tag{56}$$

is a function of location along the developing cone-jet. Close to the cone, tangential electric field dominates with a small surface charge density ($\vartheta \ll 1$); Along the jet, radial electric field eventually dominates with increasing surface charge density downstream ($\vartheta \gg 1$). The surface charge density is dependent on the detailed cone-jet dynamics. In the form of Eq. 50 with negligible gravity, q_s is governed by the imposed electric field and flow rate ($\frac{E_\infty}{E_m}$, $\frac{Q}{Q_m}$) and the associated geometrical ($\frac{z}{a}, \xi$), mechanical (We, Oh), and electrical (α, β, χ) parameters. Because of the complex, global nature of the problem, no controlling parameters (like Ra_e in Eq. 44) have emerged with appropriate scaling of the surface charge density in a developing cone-jet.

One possibility to reduce the complexity is to operate exactly at the minimum flow rate $Q = Q_m$; accordingly, it is necessary for $E = E_m$ to obtain a steady cone-jet. Unfortunately, except for the empirical scaling Eq. 49, the mechanism determining Q_m is still unknown (Fernandez de la Mora, 2007).

4.4 Pulsating cone-jet

The crucial role of the minimum flow rate (Q_m) is apparent on the operating diagram of steady cone-jets (Figure 9). In the previous section, we showed that a minimum flow rate (a critical Weber number) is necessary for the dripping to jetting transition (Eq. 55) *if* the electrohydrodynamic jet behaves analogously to its hydrodynamic counterpart. However, when $Q < Q_m$ but $E \simeq E_m$, pulsating cone-jet sets in from a supported meniscus which does not have a clear hydrodynamic analogue.

Pulsating cone-jets are also observed on charged drops (e.g. Figure 8c); see Fernandez de la Mora (2007) for a comprehensive review. For an inviscid charged drop in air, the lowest frequency of free drop oscillation (f_d) is given by Rayleigh (1882)

$$f_d = \frac{4}{\pi}\sqrt{\frac{\gamma}{\rho d^3}\left(1 - \frac{q^2}{q_R^2}\right)} \propto f_c, \tag{57}$$

where d is the diameter of the drop, q is the *total* charge on the surface, and

$$q_R = \pi\sqrt{8\varepsilon_0\gamma d^3}, \tag{58}$$

is the Rayleigh limit for the maximum electrostatic charge allowed on a static drop. Without any surface charge ($q = 0$), the frequency is simply

governed by the capillary-inertial process with a characteristic frequency of $f_c = \sqrt{\gamma/\rho d^3}$. At the Rayleigh limit, electrostatic repulsion reduces the effective surface tension to zero, leading to electrostatic fission of the drop. The electrostatic explosion can proceed through a fine fission mode *via* a cone-jet (Figure 8c and Figure 13b), or a rough fission mode into a few drops of comparable size (Fernandez de la Mora, 2007).

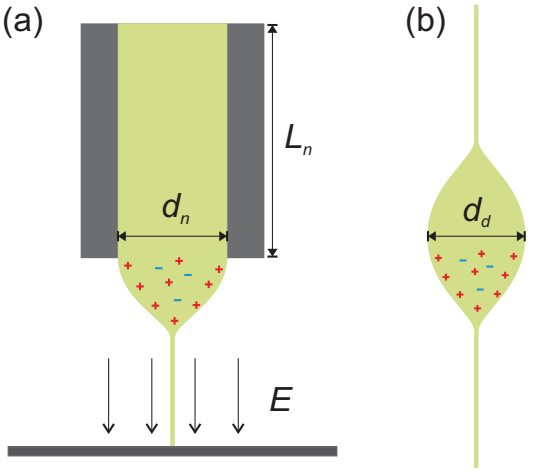

Figure 13. Analogy between pulsating cone-jets from a supported meniscus and an isolated drop: (a) The cone-jet transition under an external electric field between a nozzle and a plate; (b) The cone-jet transition when a droplet experiences electrostatic fission.

Fernandez de la Mora (1996) argued that the cone-jet pulsation on a supported meniscus is analogous to that on an isolated drop, as both result from the redistribution of the excessive electrostatic charge to a larger surface area (Figure 13).[6] When the time scale for cone-jet formation is short compared to the duration of the cone-jet, which is the case for high conductivity liquid with rapid charge relaxation, the transient cone-jet is quasi-steady and is assumed to behave similarly to a steady cone-jet on a supported meniscus (Fernandez de la Mora, 1996). Since pulsation takes place when the supply rate of liquid to the cone is less than the loss rate through the jet (Juraschek and Rollgen, 1998), a pulsating cone-jet will

[6]There are also many differences between steady and transient cone-jets, especially for liquids with high viscosity and low conductivity; see Fernandez de la Mora (2007) for details.

likely observe the minimum flow rate scaling (Fernandez de la Mora, 1996; Chen et al., 2006b). When the transient jet is on, the flow rate, jet diameter and electric current scale as (Fernandez de la Mora and Loscertales, 1994; Fernandez de la Mora, 1996; Barrero and Loscertales, 2007)

$$Q_j \sim \frac{\gamma\varepsilon}{\rho\sigma}, \tag{59a}$$

$$d_j \sim \left(\frac{\gamma\varepsilon^2}{\rho\sigma^2}\right)^{1/3}, \tag{59b}$$

$$i_j \sim g(\varepsilon)\left(\frac{\varepsilon_0\gamma^2}{\rho}\right)^{1/2}, \tag{59c}$$

where $g(\varepsilon)$ accounts for the effects of liquid dielectric constant; For aqueous solutions, $g \approx 18$ (Fernandez de la Mora and Loscertales, 1994). The lifetime of a transient cone-jet on an exploding drop can be obtained by integrating $dt = -dq/i$ (Fernandez de la Mora, 1996),

$$\Delta t_j \sim \frac{\Delta q}{i_j} \sim \frac{\Delta q}{q_R}\frac{q_R}{i_j} \sim \frac{2\sqrt{2}\pi\Delta q}{g(\varepsilon)q_R}\sqrt{\frac{\rho d^3}{\gamma}} \sim \sqrt{\frac{\rho d^3}{\gamma}} = \tau_c, \tag{60}$$

where Δt_j is the time scale for a drop with surface charge approaching the Rayleigh limit (q_R) to emit enough charge (Δq) to reach a new electrostatic equilibrium. It is generally agreed that the mass loss due to electrostatic fission is negligible (order of 1%), but the charge loss is substantial (order of 10%); see Fernandez de la Mora (1996). For water, the pre-factor in the scaling of jet duration is close to 1 (Chen et al., 2006b). Interestingly, the jetting duration (Eq. 60) reduces to the capillary-inertial time scale ($\tau_c = 1/f_c$) which also sets the oscillation frequency of an uncharged drop (Eq. 57). If the pulsating cone-jet on a supported meniscus is analogous to that on an exploding drop, the above scaling laws apply to both situations with d taken as either the drop diameter (d_d) or the *anchoring* diameter of the Taylor cone (e.g. the inner diameter of a non-wetting nozzle, d_n).

We are now in a position to reconcile two different models for the pulsating cone-jets by Marginean et al. (2006) and Chen et al. (2006b). At the onset of cone-jet pulsation, Marginean et al. (2006) observed that the pulsation frequency on a support meniscus closely follows Eq. 57 with d equal to the anchoring diameter d_n. However, the free oscillation frequency is independent of the supplied flow rate Q, and this independence contradicts with the observations in Chen et al. (2006b) as well as empirical evidences that the emergence of cone-jet pulsation strongly depends on the flow rate (see Section 4.1).

Chen et al. (2006b) proposed a different model for the pulsation frequency, motivated by the hypothesis that cone-jet pulsations result when a transient jet discharges liquid mass at a rate (Q_j) higher than the supplied flow rate (Q). For each pulsation with a duration of Δt_j, the volume of liquid extracted scales as $Q_j \Delta t_j$. By simple balance of mass flow supplied to the cone and emitted by the jet, the pulsation frequency scales as (Chen et al., 2006b)

$$f_j \sim \frac{Q}{Q_j \Delta t_j} \sim \frac{Q}{Q_m} f_c. \tag{61}$$

In other words, cone-jet pulsations result when the mass flow is limited ("choked") by upstream conditions. Note that for high conductivity fluid, the limiting factor leading to pulsation is the mass flow, not free charge, because surface charges can be generated at a rate governed the nearly instantaneous charge relaxation process. The pulsation model Eq. 61 has been confirmed by Chen et al. (2006a,b) for cone-jet pulsations with a stable conical base (see insets in Figure 14).

Xu and Chen recently showed that both models are correct within their applicable regime (Xu, 2010). In Figure 14, both laws have been identified in the same system using flow rate as the only controlling parameter. As the flow rate increases, the frequency plateaus at relatively high flow rates. Microscopic imaging indicated that the oscillation modes at low and high flow rates are fundamentally different. At low flow rates, the Taylor cone only deforms at the conical apex ("mass flow choking" regime); at high flow rates, the entire Taylor cone deforms significantly ("conical oscillation" regime). The demarcation between the two regimes is related to the minimum flow rate (Xu, 2010); For the conditions in Figure 14, $Q_m \approx 50$ μL/h according to Eq. 49.

- $Q < Q_m$: The mass flow is choked upstream, and the pulsation frequency scales as $f \sim (Q/Q_m) f_c$ (Eq. 61). The linear dependence of the pulsation frequency on the flow rate is confirmed at small flow rates (Figure 14). The mass flow choking regime is unambiguously shown by cases with self-induced flow rate (Xu, 2010), which scales inversely with the length of the slender nozzle (Chen et al., 2006b). The nozzle length (L_n) is an upstream condition that will not change the conical oscillation frequency (Eq. 57).
- $Q \gtrsim Q_m$: The conical base oscillates when ample liquid is supplied, and the frequency scales as $f \sim f_c$ (Eq. 57). The $f_c \sim d^{-\frac{3}{2}}$ scaling is verified by Marginean et al. (2006) and confirmed by Xu (2010). The diameter should be taken as that anchoring the conical base. For low viscosity liquid, the anchoring diameter can become ambiguous and a

non-wettable nozzle (such as teflon) should be used to avoid exciting the conical oscillation regime even at flow rates below Q_m.

Note that the charge relaxation time (τ_e) is 3 μs in Figure 14, an order of magnitude smaller than the 30 μs jetting duration (Δt_j) predicted by Eq. (60) and confirmed by experiments. Hence, the quasi-steady assumption holds for the transient cone-jet discussed here.

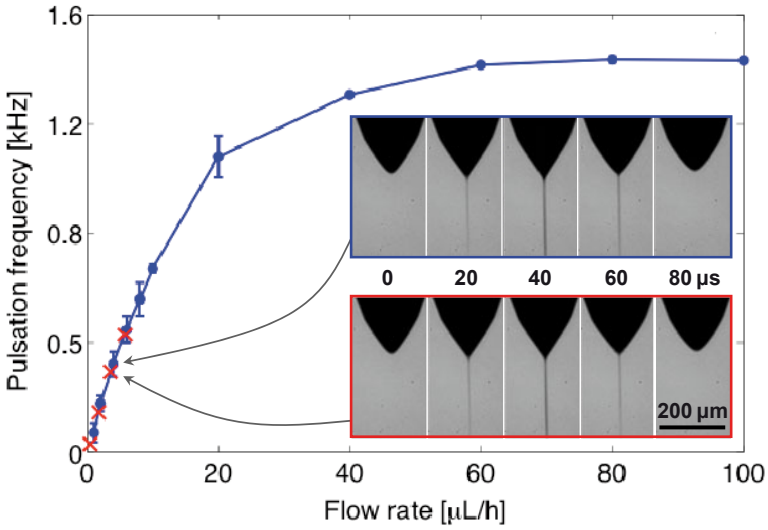

Figure 14. Pulsation frequency as a function of the imposed (•) and induced (×) flow rate. The imposed flow rate is controlled by a syringe pump, while the electric-stress-induced flow rate is varied by the nozzle length. The glass nozzle has an inner diameter of 100 μm and an outer diameter of 160 μm; here the outer diameter is the anchoring diameter. Inset shows one duty cycle of pulsation for the imposed (top) and induced (bottom) flow rate. The applied voltage of 1.8 kV is slightly lower than the threshold ($\simeq$ 2.0 kV) for a steady cone-jet. The working fluid is doped ethylene glycol with $\sigma = 1.0 \times 10^{-3}$ S/m, $\varepsilon = 3.3 \times 10^{-10}$ C/V·m, $\mu = 1.6 \times 10^{-2}$ Pa·s, $\rho = 1.1 \times 10^3$ kg/m^3, and $\gamma = 4.5 \times 10^{-2}$ N/m.

The mechanistic understanding of pulsating cone-jets has practical implications for both electrohydrodynamic printing and miniaturized electrospray. In both applications, slender nozzles with a diameter from 100 μm down to 1 μm are routinely used. The viscous drag on the slender nozzle limits the flow rate and leads to the regime of mass flow choking (Chen et al., 2006b). The intrinsic pulsations in the choking regime will influ-

ence the performance of both electroprinting and nanoelectrospray. For example, the highest speed of electrohydrodynamic printing is limited by the intrinsic pulsation frequency (Chen et al., 2006a). The advantage of nanoelectrospray over conventional electrospray diminishes with increasing flow rates (Schmidt et al., 2003); the critical flow rate is around the minimum flow rate (Eq. 49), suggesting a possible role of cone-jet pulsations in nanoelectrospray.

5 Concluding Remarks

In this chapter, electrokinetic mixing flow and electrohydrodynamic cone-jet are reviewed as two model problems of electrohydrodynamic stability. In both cases, knowledge of the stability boundary is of practical interest for either enhancing or suppressing the instability. Both problems are studied using the Ohmic model for leaky dielectrics with the assumptions of instantaneous local charge relaxation and negligible diffusive current, which hold for relatively conducting working fluids such as aqueous solutions.

The stability of electrokinetic mixing flow is relatively simple, owing in part to the well-understood base state of a diffusive interface. Using the bulk-coupled model which accounts for the electric body forces induced by conductivity gradients, a large set of relevant experimental parameters can be conveniently reduced to two controlling parameters: the electric Rayleigh number relating the dynamic to dissipative processes which governs the onset of instability, and the electroviscous-to-electroosmotic velocity ratio which governs the onset of absolute instability.

The stability of electrohydrodynamic cone-jet is significantly more difficult. Much of the difficulty is associated with the lack of a fundamental understanding of the base state, i.e. the mechanisms leading to the formation of the Taylor cone-jet. Surface-coupled model is usually employed to relate the electric and flow fields through the Maxwell stress, which now consists of contributions from both free and bound charge due to conductivity and permittivity gradients, respectively. Compared to its nonelectrical counterpart, the physics of electrohydrodynamic jets is enriched but complicated by the electric field. The most useful guideline is still the electric field–flow rate operating diagram. Strategies to rationalize the operating diagram in the framework of electrohydrodynamic stability have only been partially successful, e.g. within specific parametrical regimes of pulsating, spraying, or spinning cone-jets. Further research is required to understand key issues such as the origin of the minimum flow rate and the role of tangential electric stress before a unified theoretical picture is possible.

Bibliography

A. G. Bailey. *Electrostatic Spraying of Liquids*. Research Studies Press, 1988.

A. Barrero and I. G. Loscertales. Micro- and nanoparticles via capillary flows. *Annu. Rev. Fluid Mech.*, 39:89–106, 2007.

J. C. Baygents and F. Baldessari. Electrohydrodynamic instability in a thin fluid layer with an electrical conductivity gradient. *Phys. Fluids*, 10:301–311, 1998.

H. C. Chang and L. Y. Yeo. *Electrokinetically-Driven Microfluidics and Nanofluidics*. Cambridge University Press, 2010.

C. H. Chen, H. Lin, S. K. Lele, and J. G. Santiago. Convective and absolute electrokinetic instability with conductivity gradients. *J. Fluid Mech.*, 524:263–303, 2005.

C. H. Chen, D. A. Saville, and I. A. Aksay. Electrohydrodynamic 'drop-and-place' particle deployment. *Appl. Phys. Lett.*, 88:154104, 2006a.

C. H. Chen, D. A. Saville, and I. A. Aksay. Scaling laws for pulsed electrohydrodynamic drop formation. *Appl. Phys. Lett.*, 89:124103, 2006b.

M. Cloupeau and B. Prunet-Foch. Electrostatic spraying of liquids in cone-jet mode. *J. Electrostat.*, 22:135–159, 1989.

M. Cloupeau and B. Prunet-Foch. Electrohydrodynamic spraying functioning modes: a critical review. *J. Aerosol Sci.*, 25:1021–1036, 1994.

D. Duft, T. Achtzehn, R. Muller, B. A. Huber, and T. Leisner. Coulomb fission: Rayleigh jets from levitated microdroplets. *Nature*, 421:128, 2003.

J. Eggers and E. Villermaux. Physics of liquid jets. *Rep. Prog. Phys.*, 71: 036601, 2008.

J. J. Feng. The stretching of an electrified non-Newtonian jet: a model for electrospinning. *Phys. Fluids*, 14:3912–3926, 2002.

J. Fernandez de la Mora. On the outcome of the coulombic fission of a charged isolated drop. *J. Colloid Interface Sci.*, 178:209–218, 1996.

J. Fernandez de la Mora. The fluid dynamics of Taylor cones. *Annu. Rev. Fluid Mech.*, 39:217–243, 2007.

J. Fernandez de la Mora and I. G. Loscertales. The current emitted by highly conducting Taylor cones. *J. Fluid Mech.*, 260:155–184, 1994.

A. M. Ganan-Calvo. On the theory of electrohydrodynamically driven capillary jets. *J. Fluid Mech.*, 335:165–188, 1997a.

A. M. Ganan-Calvo. Cone-jet analytical extension of Taylor's electrostatic solution and the asymptotic universal scaling laws in electrospraying. *Phys. Rev. Lett.*, 79:217–220, 1997b.

A. M. Ganan-Calvo and J. M. Montanero. Revision of capillary cone-jet physics: electrospray and flow focusing. *Phys. Rev. E*, 79:066305, 2009.

J. M. Grace and J. C. M. Marijnissen. A review of liquid atomization by electrical means. *J. Aerosol Sci.*, 25:1005–1019, 1994.

I. Hayati, A. I. Bailey, and Th. F. Tadros. Mechanism of stable jet formation in electrohydrodynamic atomization. *Nature*, 319:41–43, 1986.

J. F. Hoburg and J. R. Melcher. Internal electrohydrodynamic instability and mixing of fluids with orthogonal field and conductivity gradients. *J. Fluid Mech.*, 73:333–351, 1976.

M. Hohman, M. Shin, G. C. Rutledge, and M. P. Brenner. Electrospinning and electrically forced jets. I. Stability theory. *Phys. Fluids*, 13:2201–2220, 2001a.

M. Hohman, M. Shin, G. C. Rutledge, and M. P. Brenner. Electrospinning and electrically forced jets. II. Applications. *Phys. Fluids*, 13:2221–2236, 2001b.

P. Huerre and M. Rossi. Hydrodynamic instabilities in open flows. In C. Godreche and P. Manneville, editors, *Hydrodynamics and Nonlinear Instabilities*. Cambridge University Press, 1998.

R. Juraschek and F. W. Rollgen. Pulsation phenomena during electrospray ionization. *Int. J. Mass. Spectrom*, 177:1–15, 1998.

P. Kebarle and U. H. Verkerk. Electrospray: from ions in solution to ions in the gas phase, what we know now. *Mass Spectrom. Rev.*, 28:898–917, 2009.

L. G. Leal. *Advanced Transport Phenomena*. Cambridge University Press, 2007.

W. G. Levich. *Physicochemical Hydrodynamics*. Prentice-Hall, 1962.

H. Lin. Electrokinetic instability in microchannel flows: a review. *Mech. Res. Comm.*, 36:33–38, 2009.

H. Lin, B. D. Storey, M. H. Oddy, C. H. Chen, and J.G. Santiago. Instability of electrokinetic microchannel flows with conductivity gradients. *Phys. Fluids*, 16:1922–1935, 2004.

J. M. Lopez-Herrera, A. M. Ganan-Calvo, and M. A. Herrada. Linear stability analysis of axisymmetric perturbations in imperfectly conducting liquid jets. *Phys. Fluids*, 17:034106, 2005.

J. M. Lopez-Herrera, P. Riesco-Chueca, and A. M. Ganan-Calvo. Absolute to convective instability transition in charged liquid jets. *Phys. Fluids*, 22:062002, 2010.

A. Manz, N. Graber, and H. M. Widmer. Miniaturized total chemical-analysis systems - a novel concept for chemical sensing. *Sensors and Actuators-B*, 1:244–248, 1990.

I. Marginean, P. Nemes, L. Parvin, and A. Vertes. How much charge is there on a pulsating Taylor cone? *Appl. Phys. Lett.*, 89:064104, 2006.

I. Marginean, P. Nemes, and A. Vertes. Astable regime in electrosprays. *Phys. Rev. E*, 76:026320, 2007.

J. R. Melcher. Electric fields and moving media. *IEEE Trans. Educ.*, E-17: 100–110, 1974. This article describes the 16 mm film by J. R. Melcher, *Electric Fields and Moving Media*, produced by the Education Development Center, 39 Chapel Street, Newton, MA.

J. R. Melcher. *Continuum Electromechanics*. MIT Press, 1981.

J. R. Melcher and W. J. Schwartz. Interfacial relaxation overstability in a tangential electric field. *Phys. Fluids*, 11:2604–2616, 1968.

J. R. Melcher and G. I. Taylor. Electrohydrodynamics: a review of the role of interfacial shear stress. *Annu. Rev. Fluid Mech.*, 1:111–146, 1969.

J. R. Melcher and E. P. Warren. Electrohydrodynamics of a current-carrying semi-insulating jet. *J. Fluid Mech.*, 47:127–143, 1971.

M. H. Oddy, J. G. Santiago, and J. C. Mikkelsen. Electrokinetic instability micromixing. *Anal. Chem.*, 73:5822–5832, 2001.

W. K. H. Panofsky and M. Phillips. *Classical Electricity and Magnetism*. Addison-Wesley, 2nd edition, 1962. Dover, 2005.

J. U. Park, M. Hardy, S. J. Kang, K. Barton, K. Adair, D. K. Mukhopadhyay, C. Y. Lee, M. S. Strano, A. G. Alleyne, J. G. Georgiadis, P. M. Ferreira, and J.A. Rogers. High-resolution electrohydrodynamic jet printing. *Nat. Mater.*, 6:782–789, 2007.

J. D. Posner and J. G. Santiago. Convective instability of electrokinetic flows in a cross-shaped microchannel. *J. Fluid Mech.*, 555:1–42, 2006.

Lord Rayleigh. On the instability of jets. *Proc. London Math. Soc.*, 10: 4–13, 1879.

Lord Rayleigh. On the equilibrium of liquid conducting masses charged with electricity. *Philos. Mag.*, 14:184–186, 1882.

D. H. Reneker, A. L. Yarin, E. Zussman, and H. Xu. Electrospinning of nanofibers from polymer solutions and melts. *Adv. Appl. Mech.*, 41: 43–195, 2007.

D. A. Saville. Electrohydrodynamics: the Taylor-Melcher leaky dielectric model. *Annu. Rev. Fluid Mech.*, 29:27–64, 1997.

P. J. Schmid and D. S. Henningson. *Stability and Transition in Shear Flows*. Springer, 2001.

A. Schmidt, M. Karas, and T. Dulcks. Effect of different solution flow rates on analyte ion signals in nano-ESI MS, or: when does ESI turn into nano-ESI? *J. Am. Soc. Mass Spectrom.*, 14:492–500, 2003.

D. P. H. Smith. The electrohydodynamic atomization of liquids. *IEEE Trans. Indus. Appl.*, IA-22:527–535, 1986.

H. A. Stone, A. D. Stroock, , and A. Ajdari. Engineering flows in small devices: microfluidics toward a lab-on-a-chip. *Annu. Rev. Fluid Mech.*, 36:381–411, 2004.

G. I. Taylor. Disintegration of water drops in an electric field. *Proc. R. Soc. London A*, 280:383–397, 1964.

M. S. Wilm and M. Mann. Electrospray and Taylor-cone theory, Dole's beam of macromolecules at last? *Int. J. Mass Spectrom.*, 136:167–180, 1994.

S. Xu. Operating regimes of self-regulated electrohydrodynamic cone-jets. Master's thesis, Duke University, 2010.

O. Yogi, T. Kawakami, M. Yamauchi, J.Y. Ye, and M. Ishikawa. On-demand droplet spotter for preparing pico- to femtoliter droplets on surfaces. *Anal. Chem.*, 73:1896–1902, 2001.

J. Zeng and T. Korsmeyer. Principles of droplet electrohydrodynamics for lab-on-a-chip. *Lab Chip*, 4:265–277, 2004.